Numerical Investigation into the Combustion Behavior of an Inlet-Fueled Thermal-Compression-Like Scramjet

Mathew G. Bricalli,* Laurie M. Brown,† and Russell R. Boyce‡
University of Queensland, Brisbane, Queensland 4072, Australia

DOI: 10.2514/1.J053513

A numerical study on the combustion behavior of an inlet-fueled three-dimensional nonuniform-compression scramjet is presented. This paper is an extension to previous work on the combustion processes in a premixed three-dimensional nonuniform-compression scramjet, where thermal compression was shown to enhance combustion. This paper demonstrates how thermal compression can be used in a generic scramjet configuration with a realistic fuel-injection method to enhance performance at high flight Mach numbers. Such a scramjet offers an extra degree of freedom in the design process of fixed-geometry scramjets that must operate over a range of flight Mach numbers. In this study, how the combustion processes are affected is investigated, with the added realism of inlet porthole fuel injection. Ignition is established from within a shock-induced boundary-layer separation at the entrance to the combustor. Radicals that form upstream of the combustor within the inlet, from the injection method, enhance combustion. Coupling of the inlet-induced spanwise gradients and thermal compression improves combustion. The results highlight that, although the fuel-injection method imparts local changes to the flow structures, the global flow behavior does not change compared to previous premixed results. This combustion behavior will be reproduced when using other fueling methods that deliver partially premixed fuel and air to the combustor entrance.

Nomenclature

A	=	area, m^2
c_p	=	pressure coefficient
D	=	diameter, m
H	=	height, m
g	=	gravity constant, m/s^2
h	=	enthalpy, J/kg
I_{sp}	=	specific impulse, /s
L	=	length, m
M	=	Mach number
$\dot{m}$	=	mass flow rate, kg/s
p	=	pressure, Pa
p_r	=	compression ratio
Re	=	Reynolds number
T	=	temperature, K
U	=	velocity, m/s
W	=	width, m
y^+	=	dimensionless wall distance
γ	=	ratio of specific heats
ϵ	=	heat addition constant
η	=	efficiency
θ	=	ramp angle, deg
ρ	=	density, kg/m^3
ϕ	=	equivalence ratio

Subscripts

c	=	combustion chamber
eb	=	local flow properties upstream of injector
h	=	high-compression side of inlet
I	=	inlet
i	=	injector
j	=	injector
ke	=	inlet kinetic efficiency
l	=	low-compression side of inlet
M	=	mixing
s	=	skew angle
t	=	total
∞	=	freestream

I. Introduction

SUPERSONIC combustion ramjets (scramjets) offer a higher potential specific impulse over rockets between the flight Mach numbers of 6 to 14, providing a more economical means of delivering payloads into orbit [1,2]. A schematic is presented in the upper part of Fig. 1, adapted from [3], of a typical scramjet engine that operates using the thermodynamic cycle (which will be subsequently detailed). The freestream is compressed by the inlet and delivered into the combustion chamber, where the fuel is injected, mixed, and burned. Combustion releases the chemical energy stored within the fuel, which raises the local enthalpy of the flow. Thrust is generated by expansion of the flow through a nozzle. Fuel can be injected either upstream in the inlet or within the combustion chamber itself, depending on the scramjet design. Shock waves generated from compression surfaces within the inlet and from fuel injection into a supersonic stream may also produce complex flow structures within the flowpath. Efficient mixing and combustion becomes challenging at high Mach numbers due to the low residence times, on the order of milliseconds, within the combustor [4].

Fixed-geometry scramjets are traditionally designed with a one-dimensional (1-D) approach in mind, where an inlet ideally delivers uniform flow properties of a certain chosen compression ratio to the combustor. In this discussion, we assume a constant dynamic pressure trajectory. At high Mach numbers, scramjets are designed to have high compression, or a high inlet contraction ratio (CR), to maximize their thrust potential. This can be understood by examining the ideal thermodynamic cycle efficiency of a scramjet engine. If we constrain the discussion to a constant-pressure heat addition process, we can see that the ideal[§] cycle efficiency [Eq. (1)] is dependent on the ratio of the operating pressure of the combustor and the ambient atmosphere. The higher the operating pressure, the higher the cycle

Received 1 April 2014; revision received 28 October 2014; accepted for publication 3 November 2014; published online 28 January 2015.

*Ph.D. Student, Mechanical and Mining Engineering, Centre for Hypersonics.

†Research Associate, University of New South Wales, Canberra, ACT 2610, Australia. Member AIAA.

‡Professor, Chair for Space Engineering, University of New South Wales, Canberra, ACT 2610 Australia. Associate Fellow AIAA.

§Isentropic compression and expansion are assumed in the inlet and nozzle, respectively.

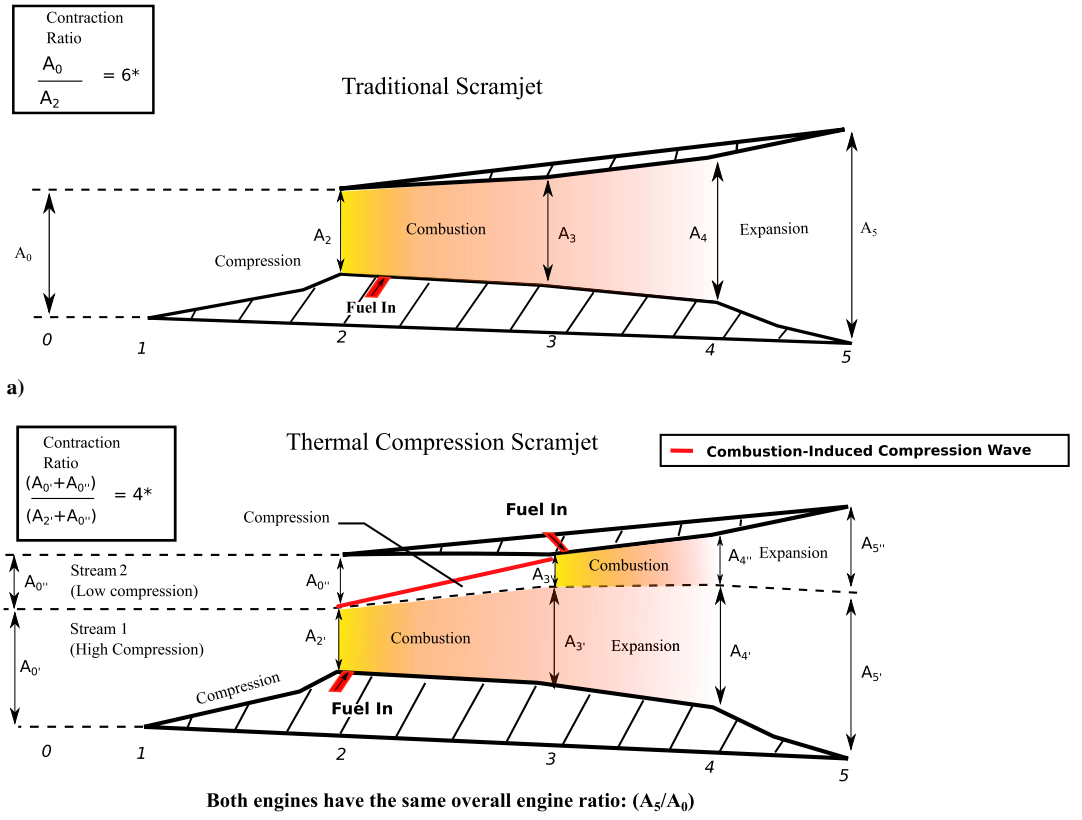

Fig. 1 Schematic of traditional one-stream scramjet and thermal compression two-stream scramjet, adapted from [3].

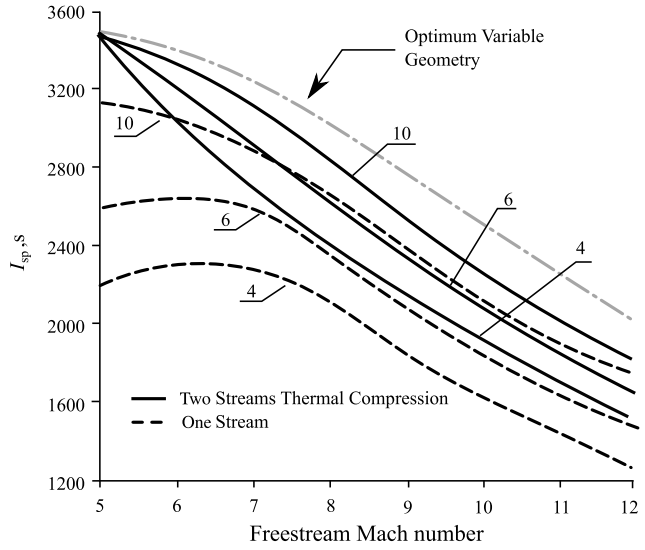

Fig. 2 Potential I_{sp} of a single-stream and a dual-stream TC scramjet, reproduced from [3], for CR of 4, 6 and 10.

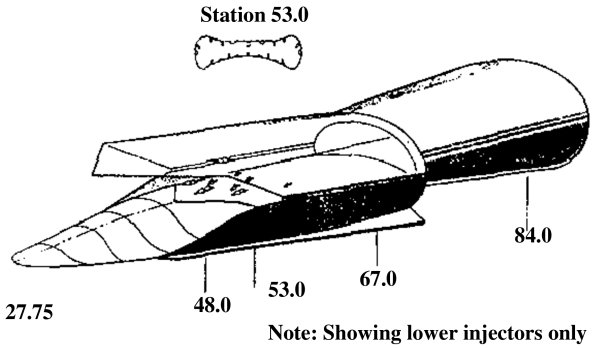

Fig. 3 Schematic of IFTV TC engine [13].

efficiency, and therefore thrust potential. (The most efficient heat addition process for a scramjet, from a thermodynamic standpoint, is the constant area to Mach 1 and then a constant Mach number to the exit of the combustor [3,5].) Combustion is often designed to take place as a constant-pressure process to minimize the structural and thermal loads on the walls of the combustor and to avoid high-pressure rises that can lead to boundary-layer separation and engine unstart [6,7]. There are practical constraints on the amount of compression an inlet should perform. These include inlet starting considerations, boundary-layer separation, excessive inlet total pressure losses with increasing CR, and nonequilibrium flow losses [8].

$$\eta_{\text{cycle}} = 1 - \left(\frac{p_\infty}{p_c}\right)^{(\gamma-1)/\gamma} \tag{1}$$

At lower Mach numbers where the flow has low compressibility, a scramjet should have lower levels of compression, or a lower CR, to prevent the engine from choking. Choking can be caused by excessive compression of the flow within the inlet, reducing it to subsonic speeds, or, thermally, from excessive heat addition that drives down the local Mach number below unity. If the CR is too high for a given Mach number, the scramjet will require a spillage mechanism or be operated at a lower equivalence ratio [5,6,9]. This will ultimately lower the performance of the scramjet. Thermal choking at low Mach numbers can also be controlled with the use of an isolator to allow both subsonic and supersonic combustion to occur; however, this increases the engine length, and therefore friction losses, es-

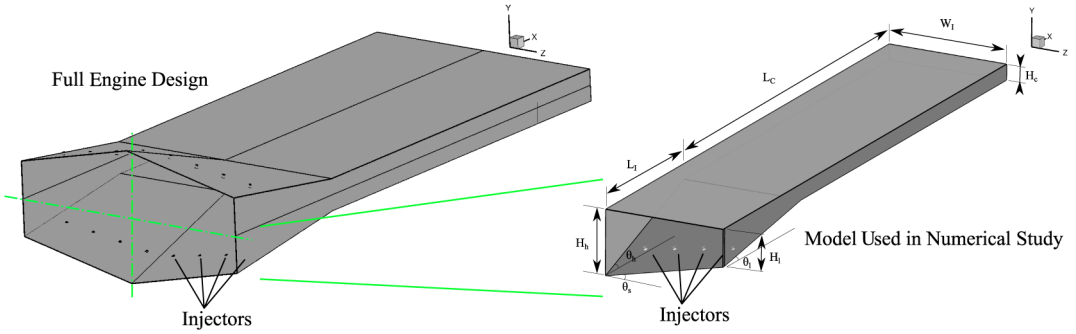

Fig. 4 3-D engine configuration.

pecially at high Mach numbers where the flow is less likely to thermally choke and the isolator is no longer required.[¶] Thermal choking can also be controlled by increasing the divergence of the combustor; however, this may result in a poorer cycle efficiency at higher Mach numbers [3].

An alternative design approach was proposed by Ferri that deliberately seeks to use three-dimensional (3-D) geometries that deliver nonuniform flow properties to the combustor [9]. Ferri claimed that 3-D nonuniform-compression engines designed to take advantage of thermal compression (TC) can provide superior performance over a range of Mach numbers [9]. Thermal compression is a heat-release/fluid-dynamic interaction where combustion that initiates in a region of high compression is used to compress flow within adjacent regions of low compression [10], thus lowering the amount of compression required by the inlet while maintaining high cycle efficiency. The TC effect is controlled by tailoring the fuel injection with combustion-induced compression waves within the combustor [10].

The potential I_{sp} gains of TC scramjets were also investigated by Billig et al. [3] using the gas-dynamic model, given schematically in Fig. 1b. In this model, stream 1 is compressed by the inlet, whereas stream 2 is compressed by combustion-induced compression waves generated from heat release in stream 1. The main findings from Billig et al.'s study are given in Fig. 2 for a constant dynamic pressure trajectory of 240 kPa. For a given inlet CR, the uninstalled I_{sp} potential of the two-stream TC scramjet is higher than a single-stream scramjet (Fig. 1a), over a range of Mach flight numbers (5–12).[**] For a CR of four, a TC engine has a theoretical performance gain of 38 and 13% at Mach 5 and 12, respectively. For a CR of 10, the gains in performance potential of the TC engine reduce to 12 and 3%. The results highlight that TC should be exploited for engines with low CRs, where low geometric compression from the inlet is compensated by TC within the combustor. The low CR feature of TC scramjets, over traditional scramjets, suggests they have better inlet starting behavior [11]. In addition, the performance gains at lower Mach numbers indicate that the total amount of fuel required to accelerate to hypervelocity speeds can be significantly reduced [3], thereby lowering the total amount of fuel required for a given acceleration trajectory.

The practicality of using TC within scramjet engines remains unanswered. Work on TC scramjet engines was first undertaken in the 1960s at General Applied Science Laboratories, where they were built and tested. One of these engines is the scramjet incremental flight test vehicle (IFTV) module, shown in Fig. 3. The engine has a tailored injection scheme that takes advantage of the nonuniform flow delivered to the combustor. The flight-test plan was to boost the vehicle to 1.65 km/s (Mach 5.5) at 17 km altitude and to demonstrate vehicle acceleration to at least 1.82 km/s (Mach 6) [12]. The flight-test program was canceled in August 1967, due to problems encountered in the ground-test program [13] associated with the control of inlet–combustor interactions [12]. Testing was performed at low supersonic Mach numbers, where the low momentum of the flow and large pressure increases associated with combustion conspired to make control difficult [14]. Ground-testing experiments, however, did achieve 80% of their thrust targets [13]. Further work on TC scramjets has not been followed through due to progress made in dual-mode engine technology, which traditionally employs uniform entry combustor conditions [12]. The occurrence of TC was reported from experiments in impulse facilities at high Mach numbers [14], where conditions are far more favorable to its exploitation [14]. Previous numerical work performed by the authors in [15] also reported that TC played a significant role in the combustion within a 3-D nonuniform-compression scramjet at Mach 10.

In addition to TC, Ferri and Agnone proposed using inlet fueling to control the combustion behavior of scramjets [16]. Inlet fueling reduces the combustor length while offering a means to control the heat-release processes by varying the fuel distribution at the combustor entrance [16]. Such a design could be used to increase the performance at high Mach numbers without the need for variable geometry. Inlet injection has shown promise in high-Mach-number scramjets such as the radical farming scramjets [17–19] and the rectangular-to-elliptical shape transition (REST) engine [20]. Radical farming scramjets typically employ nominally two-dimensional (2-D) and axisymmetric inlet compression geometries, whereas the REST engine has an inlet designed from stream tracing within an axisymmetric flowfield. There are no known examples of scramjets that combine a tailored inlet fueling method with a purposely induced, spanwise nonuniform compression to take advantage of TC.

Table 1 3-D inlet dimensions

Parameter	Value
θ_l	8.0 deg
θ_h	18.0 deg
θ_s	12.7 deg
x_j	37 mm
d_j	— —
W_I	100 mm
L_I	122 mm
L_c	328 mm
z_{j1}	12.5 mm
z_{j3}	62.5 mm
d_{j1}	2.21 mm
d_{j3}	1.95 mm
H_c	12.5 mm
H_h	53 mm
H_l	30 mm
z_{j2}	37.5 mm
z_{j4}	87.5 mm
d_{j2}	2.08 mm
d_{j4}	1.78 mm

[¶]At high Mach numbers, the isolator may be used as a constant area combustor if fuel is injected upstream or within the isolator itself.

[**]The heat addition process used in Billig et al.'s study [3] is optimized, and therefore not constrained to constant pressure.

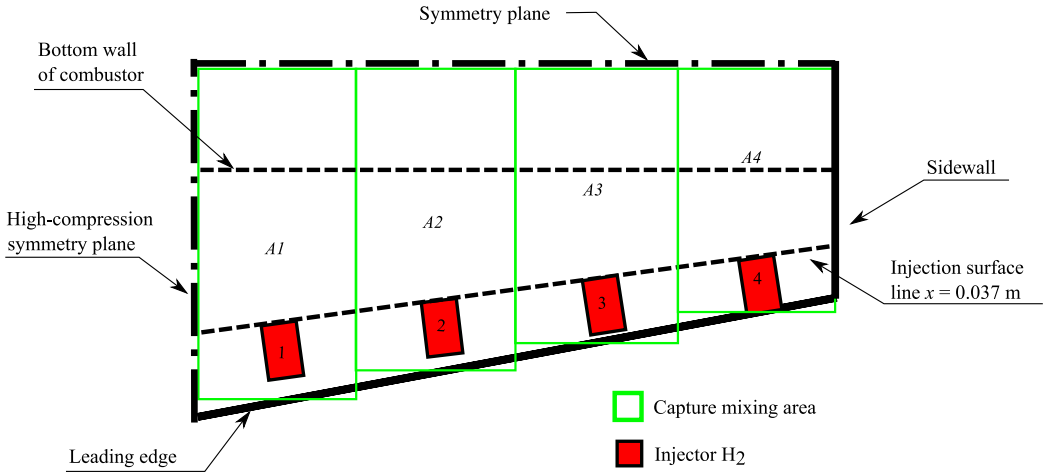

Fig. 5 Capture area used in injector sizing, flow direction is normal into page.

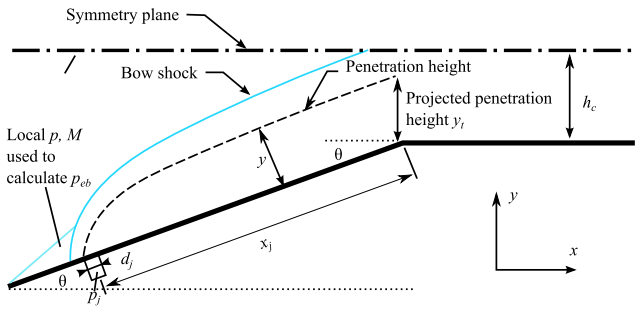

Fig. 6 Schematic of the cross section of an injector within the inlet to highlight the critical fuel penetration parameters used in Eq. (2).

The supersonic combustion processes in a premixed 3-D nonuniform-compression scramjet were characterized by the authors in [15]. That fundamental study used a premixed inflow to remove the influence of any particular fuel-injection method on the combustion processes. The 3-D inlet (Fig. 4) delivered a nonuniform-compression profile to the combustor entrance due to the varying 2-D geometric CR across the inlet. The high-contraction region located at the centerline of the engine is referred to as the high-compression side, whereas the sidewall is referred to as the low-compression side. A 2-D engine based on the dimensions of the low-compression side generates insufficient compression to ignite the flow. The high-compression side generates compression sufficient for rapid combustion [15]. That study isolated three sources of combustion enhancement in the low-compression side of the engine:

1) The first source is the 3-D flow feature, which is a shock-induced boundary-layer separation (SIBLS) that formed at the combustor entrance and provided locally high temperatures that ignited the flow.

2) The second source is radical transport, where the same SIBLS transported radicals from the high- to the low-compression sides of the engine.

3) The third source is TC, where combustion in the high compression coupled with the spanwise flow gradients to compress the flow in the low-compression region.

The premixed study is expanded upon here to investigate the combustion behavior with the added realism of fuel injection. An identical inlet geometry is used in this study with a porthole inlet injection method. The combustion chamber length is increased by 85% to allow combustion to proceed to higher levels than the premixed study. The purpose of the study is as follows:

1) Evaluate if and how TC can be used with a realistic fuel-injection method in a generic scramjet configuration.

2) Evaluate if the combustion processes of the premixed study persist, or to what extent are they were eroded or enhanced, with fuel injection.

3) Evaluate if there are performance benefits from TC effects in the generic 3-D nonuniform-compression TC-like engine relative to a generic 2-D uniform-compression engine.

This paper begins with the design of the porthole inlet injection method, based on a 1-D linearization of the capture area surrounding each injector. The nonuniform mass capture across the 3-D inlet requires a tailored fuel-injection scheme to ensure the fuel is uniformly distributed across the combustor. The uninstalled I_{sp} potential of the 3-D engine is compared to a nominally 2-D uniform-compression engine of an equivalent compression and CR to show the performance benefits of TC in the scramjet engine design. In this comparison, the 3-D nonuniform-compression engine represents a TC-like scramjet, whereas the 2-D uniform compression engine represents a traditional scramjet engine. The combustion processes

Table 2 Penetration calculations for each injector within the 3-D engine using the Povinelli and Povinelli correlation [26]

Property	Injector 1	Injector 2	Injector 3	Injector 4
θ, deg	16.75	14.25	11.25	9.25
$p_{t,j}$, kPa	1000	1000	1000	1000
p local, kPa	23	18	13	10
M local	5	5.5	6.0	6.7
p_{eb}, kPa	500	473	430	369
x_j, mm	90	89	88	87
d_j, mm	2.20	2.10	1.94	1.78
y_t, mm	10.22	10.0	9.76	9.77
y_t/h_c	0.81	0.79	0.78	0.78

Table 3 Freestream conditions

Parameter	Value
M_∞	10
U_∞	3000 m/s
p_∞	1450 Pa
T_∞	227 K
ϕ	0.99
$T_{t,\infty}$	4767 K
$p_{t,\infty}$	61 MPa
$h_{t,\infty}$	4.5 MJ/kg

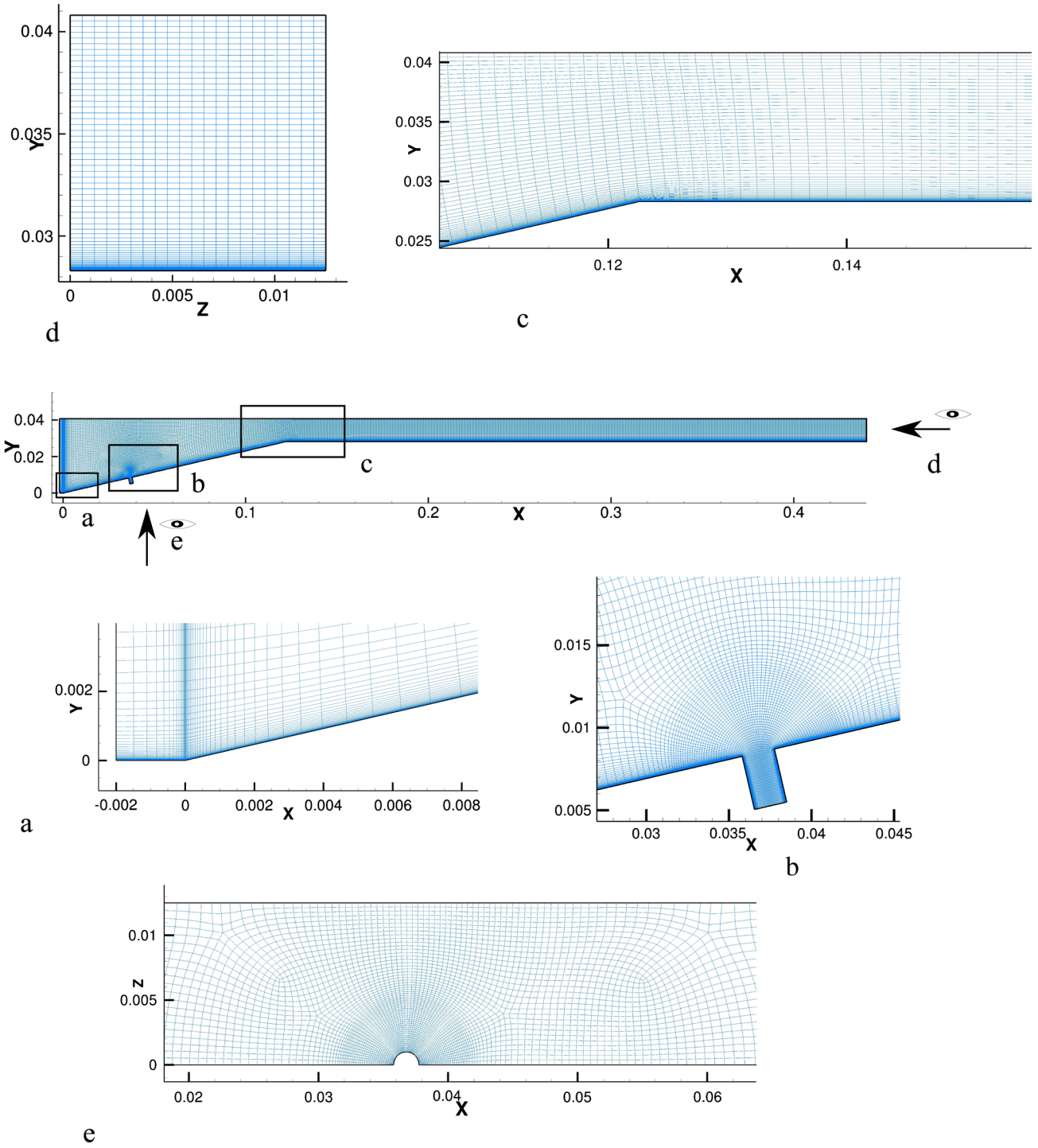

Fig. 7 Coarse mesh topology of nominally 2-D engine.

are then isolated within the flowfield by artificially suppressing reactions in local regions in the combustor following the method used in [15]. A second method to investigate the coupling behavior of the spanwise flow gradients and combustion involves injecting combinations of hydrogen and inert hydrogen (nonreacting) within the high- and low-compression sides of the engine. The latter method enables us to isolate how the combustion of fuel injected into the low-compression side proceeds without the influence of combustion from fuel injected in the high-compression side, or vice versa. As will be shown, the ignition processes within the inlet-fueled 3-D engine are more complex compared to those identified in the premixed study, owing to the additional shock structures and mixing processes from fuel injection. However, the global spanwise flow gradients/TC combustion coupling behavior, which was also identified in the premixed, persists.

II. CFD++

The CFD simulations presented in this paper were performed using CFD++, developed by Metacomp Technologies [21]. CFD++ can provide unsteady- and steady-state solutions to the Navier–Stokes equations for compressible and incompressible flows with multi-species and finite-rate chemistry modeling. CFD++ uses a multi-domain unstructured solver capable of handling Cartesian, structured

curvilinear and unstructured grids, including hybrids with various cell topologies. The code uses a total variation diminishing discretization method based on a multidimensional interpolation framework. The upwind Harten–Lax–van Leer–contact Riemann solver provides proper signal propagation physics at flow discontinuities. For the near-wall turbulence closure, the solve-to-the-wall method is used.

A variety of turbulence models are available in CFD++, ranging from conventional Reynolds-averaged Navier–Stokes (RANS) one- to seven-equation transport models to large-eddy simulation (LES) models and hybrid RANS/LES models. The shear stress transport (SST) model is used to simulate turbulence in all scramjet calculations presented in this study [22]. The SST turbulence model has been shown to accurately capture supersonic flow phenomena, such as shock/boundary-layer interactions (SBLIs) and mixing processes from injecting fuel into supersonic crossflows [23,24]. With all calculations, turbulence production and dissipation terms are corrected to include compressibility effects using the proprietary method formulated for CFD++. Combustion is simulated using the 13-species 33-reaction hydrogen-air finite-rate model of Jachimowski [25] that was developed in the context of the U.S. National Aero-Space Plane program. Turbulence-chemistry interactions are excluded in this work. A fully structured computational domain is used for all scramjet simulations, taking advantage of symmetry planes in each configuration. Time integration is performed using the implicit Euler method using local time stepping, and the solution is run to steady state.

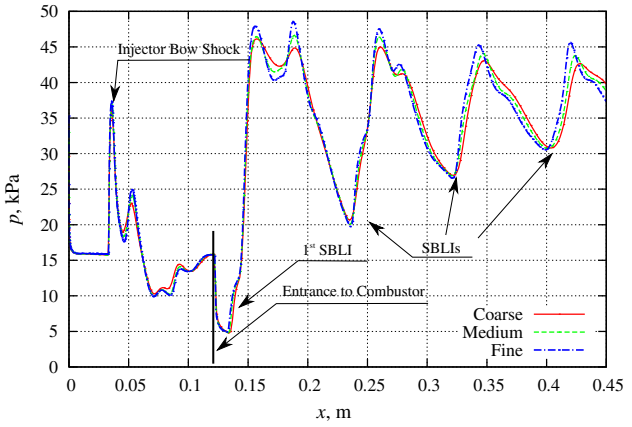

a) Frozen flow

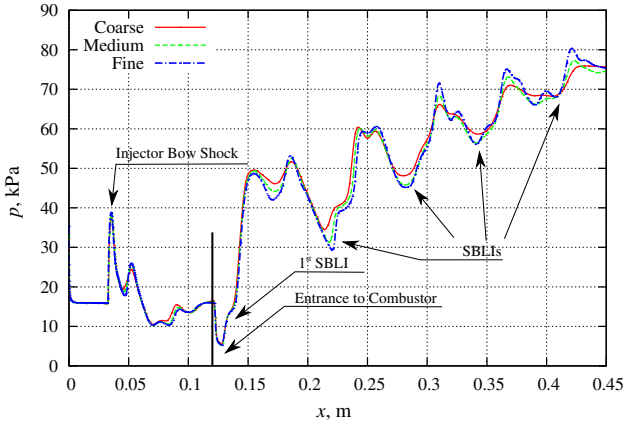

b) Reacting flow

Fig. 8 Pressure along combustor at midspan of computational domain, $z = 6.25$ mm.

III. Engine Design

The 3-D engine geometry and dimensions are given in Fig. 4 and Table 1. The geometry consists of a single-ramp planar symmetric inlet with a rectangular constant cross-sectional area combustion chamber. This geometry is selected to make the numerical solution performed here easily applicable to experimental investigation, by providing opportunity for flow visualization in ground-test facilities such as the University of Queensland's T4 hypersonic reflected shock tunnel. The 3-D inlet geometry is based on the design detailed in [15]. The high- and low-compression profiles consist of 18 and 8 deg single ramps with 2-D CRs of 2.37 and 4.18, respectively. The inlet contains 16 evenly spaced injectors along the bottom and top walls at 30% of the inlet length downstream of the leading edge. The nominally 2-D model used to compare the performance of the 3-D model has a ramp angle of 13 deg and a CR of 3.28. The CRs of both the 3-D and 2-D inlets are within 1%, and the mean compression ratios are within 4%.

The injectors are tailored to deliver an equivalence ratio of one across the engine. The plenum pressure and temperature are set to 1 MPa and 300 K for all injectors. Fueling is tailored based on the capture area surrounding each injector and the injector diameter. This is shown schematically in Fig. 5 for the 3-D engine. The injectors of the 3-D engine, starting from the high- to low-compression sides, have areas of 3.83, 3.40, 2.98, 2.51 mm^2 respectively. The 2-D engine injectors have an area of 3.14 mm^2 evenly spaced across the inlet. The injectors are aligned perpendicular to the local surface of the inlet. Optimization of the arrangement to achieve better mixing and lower total pressure losses is not pursued in this study.

The penetration height of fuel into the supersonic stream for each injector in the 3-D engine is checked using the correlation of Povinelli and Povinelli [26], given in Eq. (2). This version of the correlation neglects the effects of the boundary-layer thickness, which is assumed to be approximately the same across the inlet. The penetration height y at some downstream location x is calculated based on the injector diameter d_i, the ratio of the total pressure of the fuel $p_{t,j}$, and the "effective backpressure" p_{eb}, defined as two-thirds of the total pressure behind a normal shock in the flow upstream of the injector. M_j corresponds to the exit jet exit Mach number, which is one for choked flow. These parameters are shown schematically in Fig. 6. The properties upstream from each injector are not constant, due to the varying ramp angles in the spanwise direction of the inlet; therefore, p_{ab} must be calculated for each injector based on the local flow properties.[††] The 3-D engine calculations are summarized in Table 2. The predicted fuel penetration height for each injector is within 3% when normalized with the combustor height. The data highlight that the injector sizing methodology used here is suitable for this class of inlet geometry. As will be shown in the sections that follow, this fueling arrangement delivers approximately the same mixing efficiency, fuel penetration, and distribution for both the 3-D and 2-D engines to the combustor entrance:

$$\frac{y}{d_i} = 1.12\left(\frac{p_{t,j}}{p_{\text{eb}}}\right)^{0.483}(M_j)^{0.149}\left(\frac{x}{d_j}+0.5\right)^{0.281} \tag{2}$$

IV. Boundary Conditions

The freestream inflow conditions given in Table 3 correspond to a Mach 10 flight condition at an altitude of 30 km, with a freestream dynamic pressure of 100 kPa. The freestream turbulence is set to 2%, with a laminar-to-turbulent viscosity ratio of two. The outflow is set to supersonic outflow. The short test times, in impulse facilities, are insufficient to cause a significant rise in wall temperature. Therefore, the walls are modeled as nonslip isothermal walls at 300 K. The injector boundary conditions are set to an inflow of H_2 with a stagnation pressure and temperature of 1 MPa and 300 K.

[††]These values are taken from the fueloff computational fluid dynamics solution presented in the sections that follow.

V. Mesh Sensitivity Study with the Two-Dimensional Scramjet Configuration

A mesh sensitivity study is performed to ensure the combustion processes investigated in the sections that follow are mesh independent. The study is conducted on the nominally 2-D engine with a compression ramp angle of 13 deg. Three meshes (coarse, medium, and fine) are used with a refinement factor of 1.5 in each dimension. The mesh topology is given in Fig. 7 and is generated using GRIDPRO [27]. Cells are clustered to the walls to 0.75, 0.5, and 0.33 μm with a growth factor of 1.2 for the coarse, medium, and fine meshes. The coarse, medium, and fine meshes contain 1 million, 3.4 million, and 11.4 million cells, respectively. The y^+ values are below 0.8 over all wall surfaces. Cells are clustered around the injectors, as shown in Fig. 7b, to ensure that the supersonic jet interaction flow structures are resolved.

Both temporal and mesh convergences are addressed. Each simulation reached temporal convergence after the mass, momentum, and energy residuals reduced by five orders of magnitude. As will be discussed in the sections that follow, a shock-induced boundary layer separation at the entrance of the combustor plays an important role in igniting the flow. The size of the separation was therefore used as a metric for determining temporal convergence. In all simulations, sufficient iterations were run so that the size of the separation stabilized.

Mesh convergence is assessed by comparing the temporally converged numerical solutions for the coarse, medium, and fine meshes. Pressure data are extracted from the bottom wall at the midspan of the computational domain in Fig. 8. The pressure data show that the locations of the SBLIs do not vary significantly between each mesh in both the frozen and reacting simulations. There are differences in the peak pressure values between the meshes at the SBLIs. The coarse and medium meshes consistently underresolve the peak pressure value by about 5 and 2.5%, respectively, relative to the fine mesh. Furthermore, the locations of the SBLIs are displaced toward the exit of the combustor compared to the fine mesh. The pressure data show that the flow is asymptoting to a mesh-independent solution, with further mesh refinement unnecessary to resolve the important flow physics. This indicates that heat-release rates are not changing with mesh refinement.

Mixing processes within the inlet are also compared in the constant H_2 contour profiles at the entrance of the combustor in Fig. 9. The calculated mixing efficiencies, adopted from [28], at the entrance of the combustor are 26, 24, and 23% for the coarse, medium, and fine meshes, respectively. The reduced resolution of the fuel plume transport through the inlet within the coarse and medium simulation results in a higher mixing efficiency compared with the fine grid.

The constant atomic H mass fraction and H_2O combustion efficiency contours at the entrance and exit of the combustor are given in Figs. 10 and 11, respectively. (The definition of combustion efficiency used here is the ratio of the actual H_2O mass fraction to the stoichiometric H_2O mass fraction, for an equivalence ratio of one.) All meshes show intermediate combustion species (radicals) at the entrance of the combustor. The atomic H plume given in Fig. 10 becomes more condensed with increasing cell density. The SIBLS at the first SBLI immediately downstream from the combustor is compared between each mesh in Fig. 12. The bottom wall has been flooded with atomic H mass fraction contours and limiting streamlines plotted on the surface using the shear stress vector, which show the size of the recirculation bubble. All simulations show a maximum H mass fraction of 0.0065 and the same separation length.

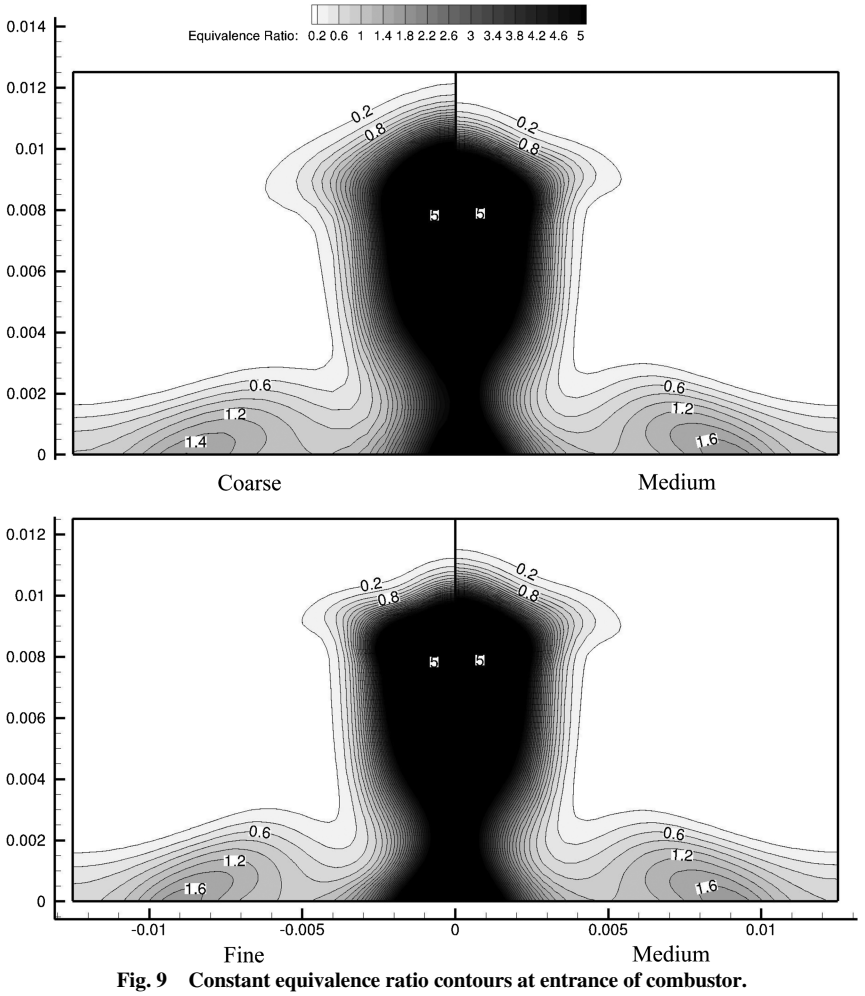

Fig. 9 Constant equivalence ratio contours at entrance of combustor.

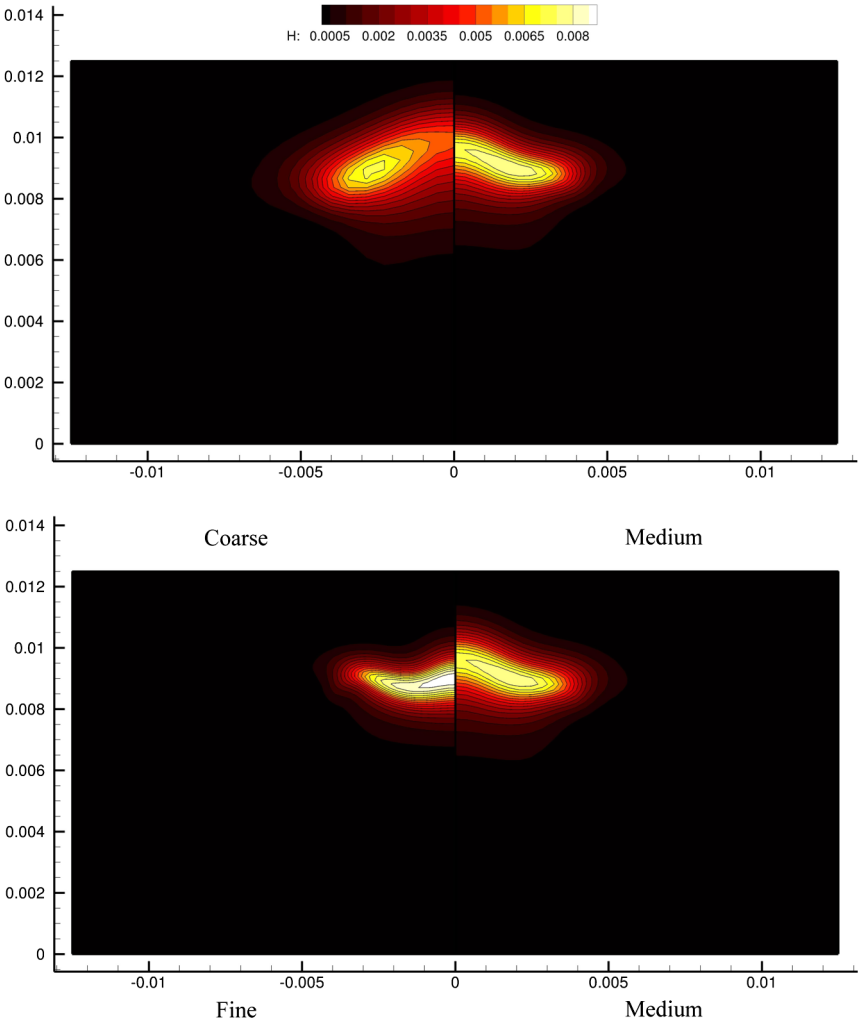

Fig. 10 Constant atomic H mass fraction contours at entrance of combustor.

The ignition process within the first SBLI is therefore consistently captured in each mesh.

The mesh sensitivity study shows that the pressure rise and combustion processes do not change with mesh refinement. The coarse mesh therefore sufficiently resolves the flow structures and combustion processes necessary for this work. The solutions presented in the sections that follow use the same mesh topology and cell density as the coarse mesh.

VI. Two-Dimensional Results

The results for the 2-D engine are given in Figs. 13, 14, and 15. A comparison of the pressure coefficient contours [Eq. (3)], given in Fig. 13a for the frozen and reacting flow, shows there is a significant pressure rise from combustion. The shock structure in the combustor changes with reactions activated, as shown by the change in location of the SBLIs in Fig. 13b. This is due to the influence of the reactions, which lowers the Mach number, and therefore alters the shock structure.

$$c_p = (p - p_\infty)/\left(\frac{1}{2}\rho_\infty U_\infty^2\right) \tag{3}$$

The porthole injection method generates the typical flow structures expected from sonic injection into a supersonic crossflow, detailed in Fig. 14 at the symmetry plane, that serve to enhance the near-field mixing. Far-field mixing is controlled by turbulent diffusion and is enhanced when the flow passes through shock waves, owing to baroclinic torque generated from the pressure and density gradients of the plume and air. In the interest of brevity, the mixing processes are not detailed further; however, further discussion on the mixing processes in inlet-fueled scramjets can be found in [29,30].

Figure 15 shows the combustion efficiency and temperature contours in the engine for the reacting simulation. The bottom wall is flooded with the pressure coefficient, with the shear stress topology superimposed. The high temperature, in excess of 1600 K, produced in the mixing layer of the fuel and air causes the flow to react and form radicals. This phenomena was reported in an experimental investigation of porthole fuel injection into supersonic flow [31]. An inherent limitation of the turbulence modeling in RANS simulations is its inability to capture the small-scale turbulent eddies, and therefore the combustion process, within the free shear layer of the jet. It will be shown in the sections that follow that the suppression of reactions in the inlet does not alter the global combustion behavior.

The SIBLS at the first SBLI, shown in Fig. 12, ignites the flow within the boundary layer. The recirculation region between the injectors contains partially mixed fuel and air at temperatures in excess of 1400 K, as shown in Fig. 15. Fuel and air entrained into the separation react to produce radicals, which diffuse out of the recirculation zone and into the boundary-layer reattachment region. This flow feature acts as a flameholder, which ignites the flow around the outer edge of the plume along the bottom wall. Radicals formed within the inlet around the upper part of the H_2 plume ignite the flow in that region after passing through the reflected shockwave off the symmetry plane. Combustion that is initiated within the outer mixing region of the plume propagates inward via a diffusion controlled heat-conduction process [9], due to the partial mixing of fuel and air within

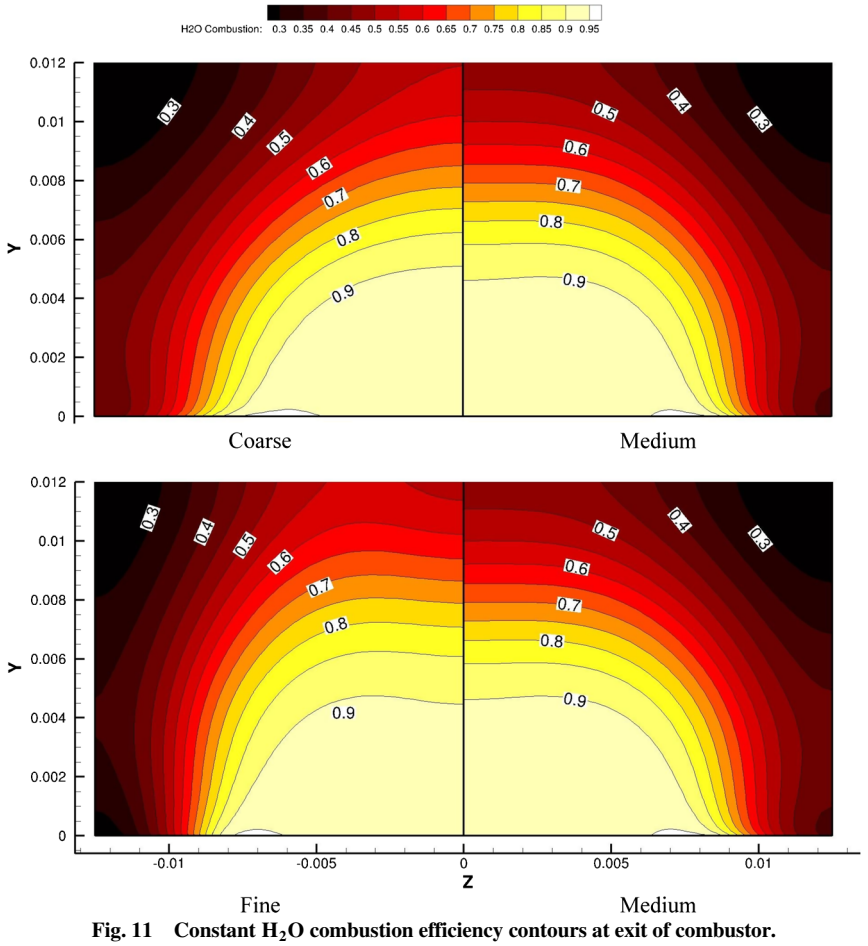

Fig. 11 Constant H_2O combustion efficiency contours at exit of combustor.

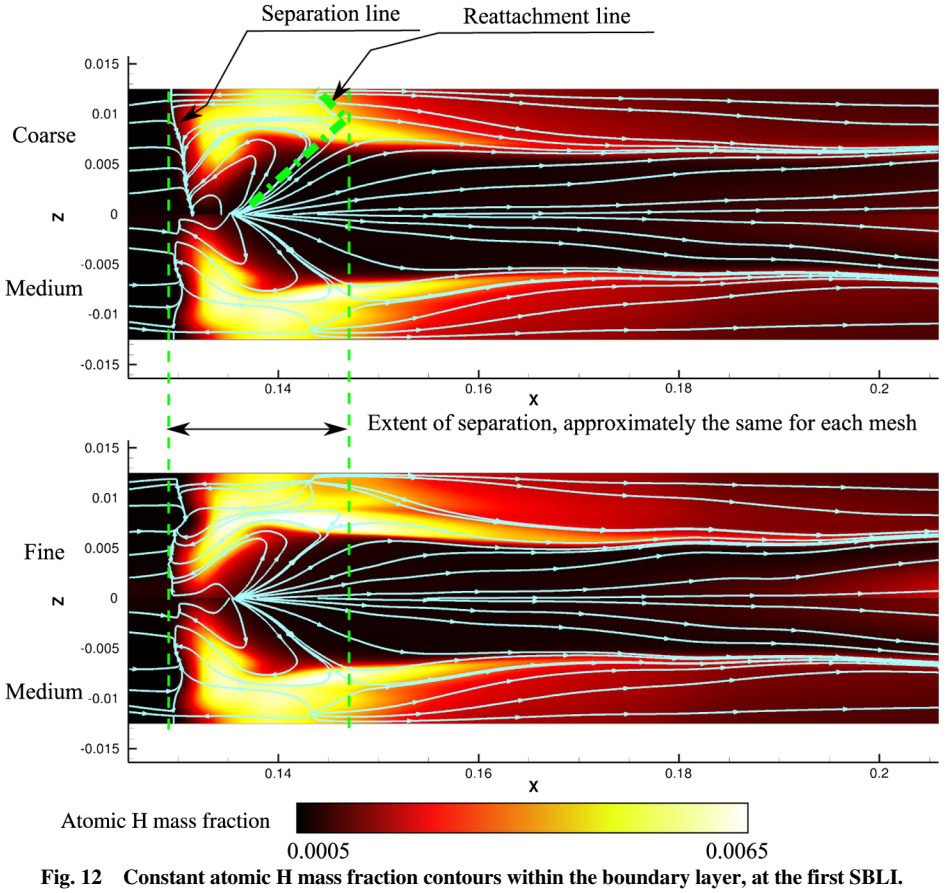

Fig. 12 Constant atomic H mass fraction contours within the boundary layer, at the first SBLI.

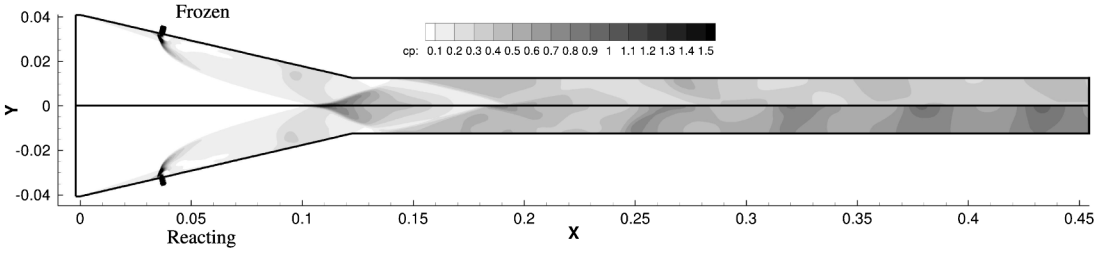

a) Injector symmetry plane pressure coefficient contours, frozen (top) and reacting (bottom)

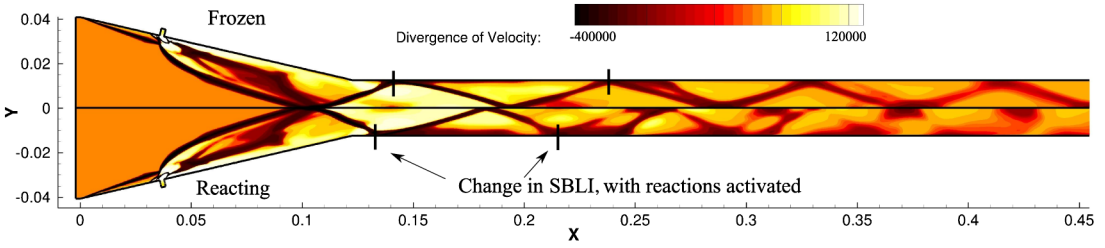

b) Shock structure at symmetry plane of 2-D engine: frozen (top), reacting (bottom); flooded with divergence of velocity

Fig. 13 2-D scramjet flowfield.

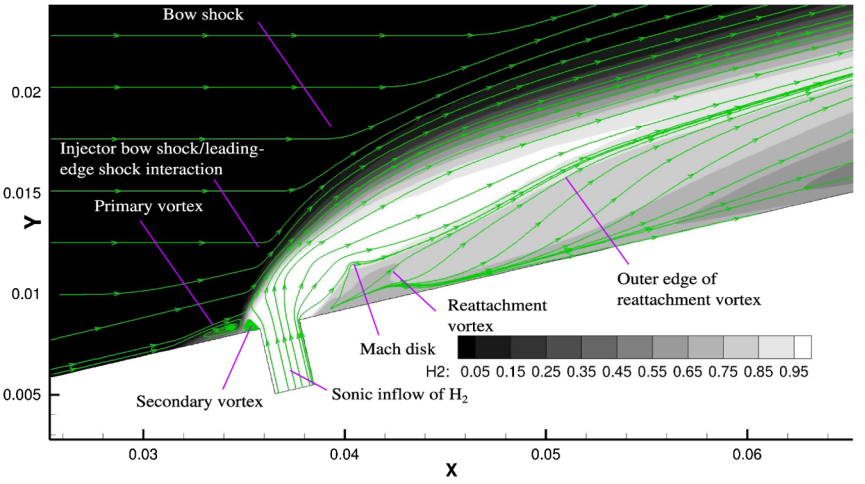

a) H_2 mass fractions and streamlines at symmetry plane

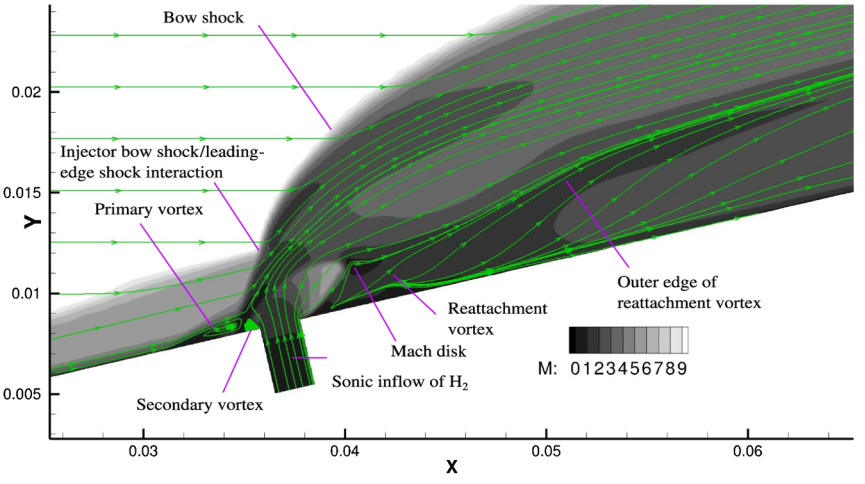

b) Mach number and streamlines at symmetry plane

Fig. 14 Flow features generated from inlet sonic fuel injection in the 2-D engine.

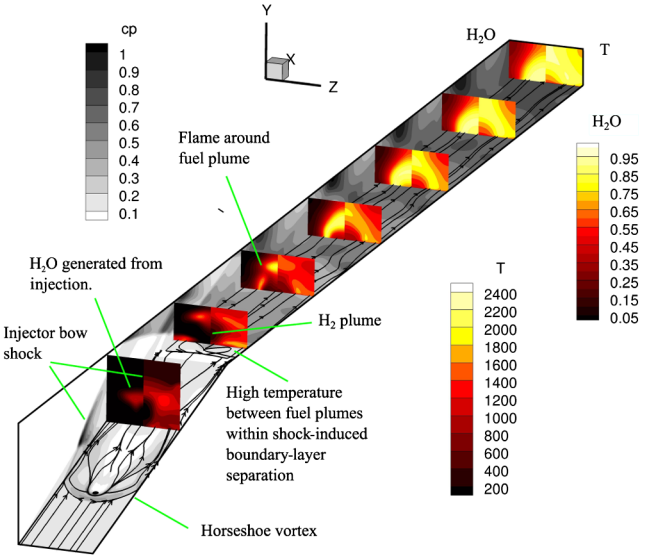

Fig. 15 2-D engine: Reacting flow. Cross-stream slices of H_2O Combustion (left), temperature (right).

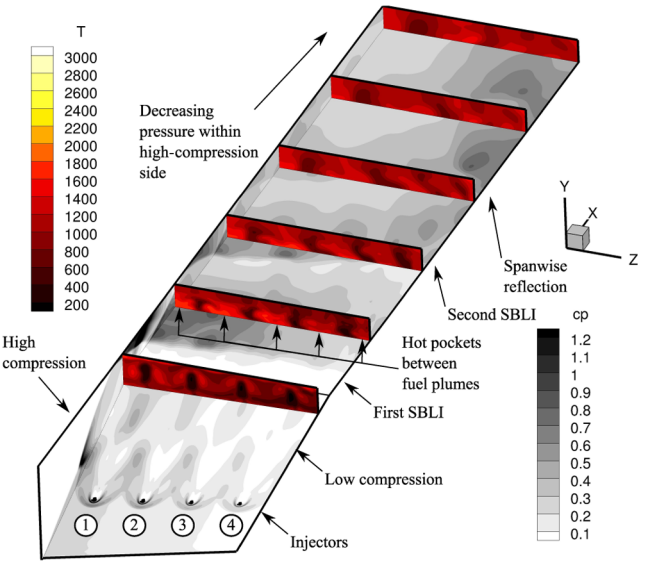

a) Frozen flow: Constant temperature contours, bottom walls flooded with constant pressure coefficient

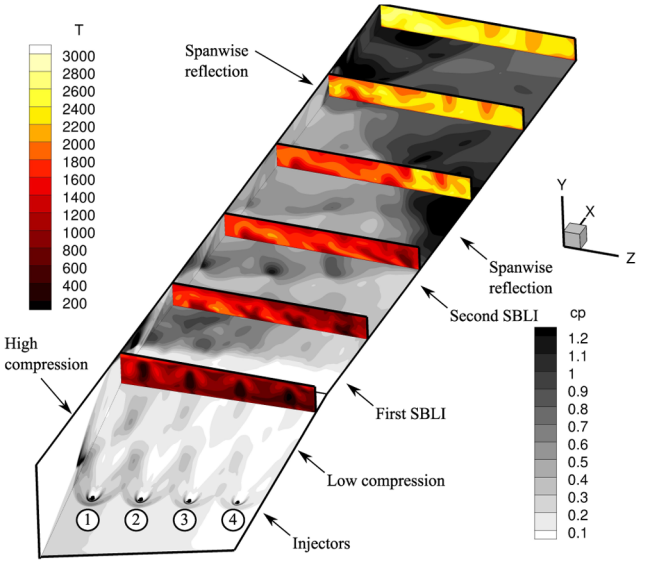

b) Reacting flow: Constant temperature contours, bottom walls flooded with constant pressure coefficient

Fig. 16 3-D engine results.

the inlet. High levels of combustion (56%) are achieved at the exit of the combustor.

VII. Three-Dimensional Results

The temperature and pressure in the 3-D engine for the fuel-on frozen and reacting simulations are presented in Fig. 16. The cross-stream slices are flooded with constant temperature contours, whereas the bottom walls and high-compression symmetry plane ($z = 0$) are flooded with the constant-pressure coefficient. Combustion in the 3-D engine increases the temperature and pressure and alters the shock structure. The nonuniform-compression flowfield contains streamwise SBLIs (as in the 2-D results) and spanwise shock reflections, detailed in Fig. 16. Unlike in the frozen simulation, the spanwise shock reflection in the low-compression side traverses the flowfield into the high-compression side with reactions enabled. This highlights the coupling of combustion with the inlet-induced spanwise flow gradients to be discussed in this section.

Figure 17a shows the cross-stream slices of H_2O combustion efficiency in the engine. Figure 17b shows the H_2O combustion efficiency and shear stress topology within the boundary layer. As in the 2-D simulation, the flow is ignited around the fuel plumes at the combustor entrance due to the combination of high temperatures generated from the separation along the bottom wall and radicals produced in the shear layer of the fuel and air in the inlet. Higher levels of combustion are achieved immediately downstream from the first SBLI within the high-compression side of the engine, owing to the higher local pressure and temperature. Combustion in the low-compression side is lower immediately downstream from the first SBLI; however, high levels are produced after the second SBLI.

The 3-D inlet delivers the intended nonuniform inflow profile into the combustor, as shown in a cross-stream slice taken upstream of the combustor entrance in Fig. 18a. The constant equivalence ratio contours at the entrance to the combustor (Fig. 18b) show that the flow has been partially mixed within the inlet and the penetration height of the fuel is about the same for each fuel plume. The influence of the porthole injection method on the global flow behavior is shown in Fig. 19, where the surface (or wall) shear stress topology and constant-pressure contours of the fueloff and frozen fuel-on simulations are compared. The SIBLS at the entrance of the combustor changes from smooth, without fuel injection, as in the premixed study in [15], to corrugated, with fuel injection. These changes are due to the additional shock waves generated by the porthole injection method (Fig. 18a) and associated mixing processes. The shocks generated from the injectors merge with the inlet leading-edge shock, as shown in the 2-D shock structure in Fig. 13b, and steepen the shock wave that enters the combustor. This causes the SBLI at the entrance of the combustor to move upstream relative to the fueloff case and increases the number of streamwise SBLI. Two local high-compression regions form along the bottom wall of the combustor. The first is within the high-compression side of the combustor ($z = 0$) at the first SBLI, which is expected owing to the inlet design. The second is within the low-compression side of the scramjet at $x = 0.38$ m, which is generated by the spanwise reflection. Compression waves from the high-compression region at the entrance of the combustor traverse the engine in the spanwise direction into the low-compression region. The waves are terminated by a reflection off the sidewall (spanwise reflection) between the second and third SBLIs, as shown in Fig. 20a. This behavior is present in both the frozen fuel-on and fueloff simulations, which indicates the inlet fueling method does not change this spanwise flow behavior.

The influence of the combustion on the flowfield is illustrated in Fig. 20a, where the shear stress topology and pressure contours along the bottom wall of the engine are plotted for the fuel-on frozen and reacting simulations. The pressure and shear stress data extracted

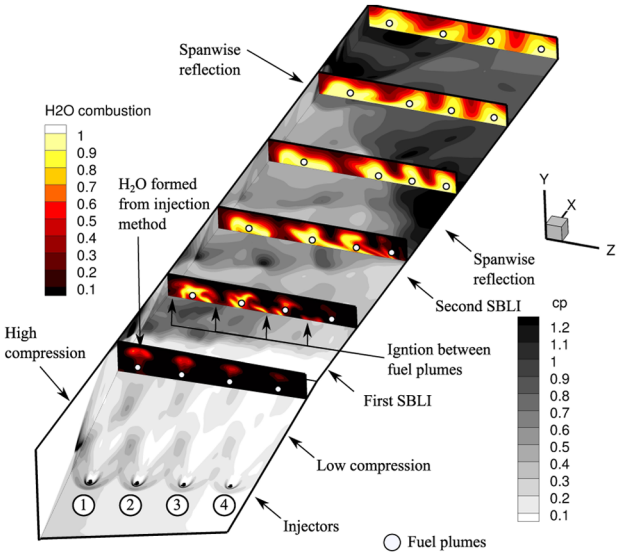

a) Slices flooded with constant H_2O combustion efficiency, and bottom wall flooded with pressure coefficient

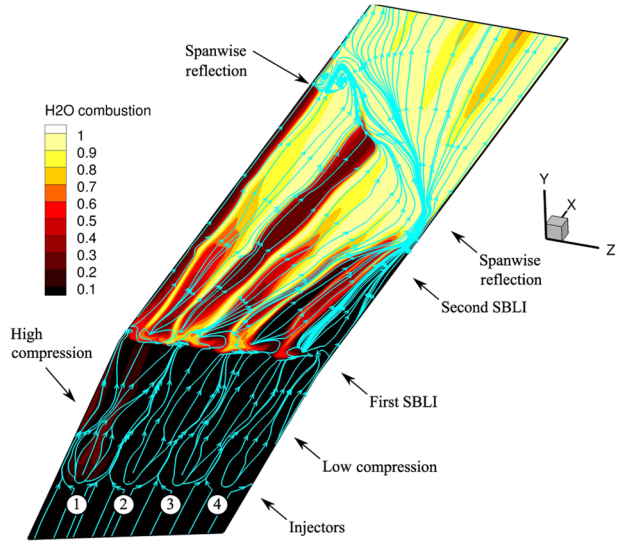

b) Bottom wall shear-stress topology, and flooded with H_2O combustion efficiency

Fig. 17 3-D results: reacting flow.

from the midspan of the computational domain are given in Fig. 20b and 20c, respectively. The streamwise length of the SIBLS (indicated by the negative x component of the shear stress in Fig. 20c) at the entrance of the combustor increases by 20% when reactions are enabled. The spanwise reflection at the low-compression side moves further upstream, whereas unlike in the fuel-on frozen simulation, the spanwise shock reflection at the sidewall rapidly traverses the flowfield back into the high-compression region. The local pressure coefficient increases from 0.55 to 0.98 (44%) over the spanwise reflection shock wave, as shown in Fig. 20b. This results in an incipient boundary-layer separation, as shown in Fig. 17b. These changes can be explained by the increased adverse pressure gradient from combustion downstream of the separation. The increase in temperature also reduces the Mach number and steepens the shock angles relative to the wall, thus inducing a larger pressure gradient, and therefore larger separation. The decreased Mach number also allows greater spanwise communication of pressure rise and increases the spanwise reflection angle. If a constant pressure is assumed through the boundary layer, the increased temperature decreases the density, and hence the momentum of the incoming boundary-layer, making it more susceptible to separation for a given adverse pressure gradient. The increased boundary-layer temperature also reduces the Mach number through the boundary layer, allowing greater upstream communication.

Another feature of the 3-D flow is the spanwise movement of the fuel plumes in the combustor, shown in Fig. 17a. The plumes within the high-compression (injectors 1 and 2) region move toward the low-compression side after the first streamwise SBLI as they follow the local favorable pressure gradient generated from the inlet. At the exit of the combustor, the combustion plumes are approximately realigned with their original spanwise injector locations in the inlet. Note that the H_2O in the boundary layer (see Fig. 17b) does not accurately represent the plume movement within the core flow. This is because the low-momentum flow within the boundary layer is more susceptible to pressure gradients.

Although RANS turbulence models can predict the mixing within inlet-fueled scramjets [29], each turbulence model will predict different levels of mixing and may require parameters such as the turbulent Schmidt number to be calibrated (see [24], for example). This variability is inherently due to the inability of RANS to capture unsteady turbulent eddies. This also applies to capturing the unsteady characteristics of SIBLSs. Caution must therefore be exercised when using RANS to simulate mixing and combustion processes.

The engine is simulated using the Spalart–Allmaras (SA) turbulence model [32] to ensure the flow behavior is not dependent on the selected SST model only. A comparison of the SST and SA simulations is presented in Fig. 21, where the H_2O combustion efficiency within the boundary layer is shown with the shear stress topology. The simulations show that the spanwise flow gradient/combustion coupling behavior is unchanged, and is therefore not unique to the SST turbulence model. Both simulations show about the same SIBLS size at the first SBLI; however, the SA solution predicts fewer radicals in the low-compression side of the scramjet. Furthermore, the boundary-layer separation at the spanwise reflection within the high-compression side of the combustor is not predicted in the SA solution. Despite these differences, the physical processes that facilitate ignition and combustion do not change when using either turbulence model. Therefore, it is expected that the combustion behavior will be reproduced when using other turbulence models.

VIII. Comparison of the Two-Dimensional Uniform and Three-Dimensional Nonuniform-Compression Engine

The stream thrust average (STA) pressure coefficient and combustion efficiency in the 2-D and 3-D engines are given in Fig. 22. (The 3-D engine results presented in Table 22 and Figs. 22 and 23 have the low-compression sidewall modeled as an inviscid slip wall. This is because the nominally 2-D engine does not contain sidewalls. The drag introduced from the sidewall in the 3-D engine must therefore be removed to make a fair comparison between the two engines.) Details on the STA computations can be found in [33,34]. The 3-D and 2-D geometries produce inlet pressure ratios of 22.5 and 23.5, respectively, which show they have approximately the same compression ratio. The pressure rise, or rate of combustion, within the 2-D engine proceeds quasi linearly. The pressure rise in the 3-D engine proceeds linearly at the start of the combustor between 0.123 and 0.25 m; however, between 0.25 and 0.3 m, there is an increase in the rate of pressure rise. This increase occurs at the second SBLI location ($x \approx 0.25$ m). After 0.3 m, the rate of pressure rise reduces; however, it remains higher than that of the 2-D engine. The same trend is given in the combustion efficiency, as shown in Fig. 23.

Figure 24 compares the uninstalled I_{sp} of the 2-D and 3-D engines. The uninstalled I_{sp} is calculated using Eq. (4), using the STA properties at a given streamwise x cross section, shown schematically in Fig. 25. Expressing the uninstalled I_{sp} in this form enables the drag within the inlet, injection method, and combustor to be compared. The change in uninstalled I_{sp} in the combustor is approximately the same for both engines, which indicates that the flow nonuniformity does not increase the drag in the combustor:

$$I_{sp} = [(\dot{m}_x U_x - \dot{m}_0 U_0) + A_x(p_x - p_0)]/\dot{m}_{H_2} g \qquad (4)$$

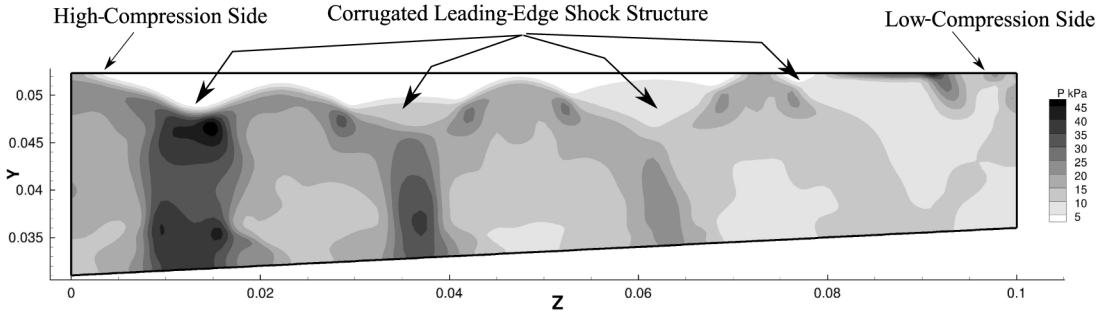

a) Slice upstream of combustor (x = 0.095 m): pressure contours

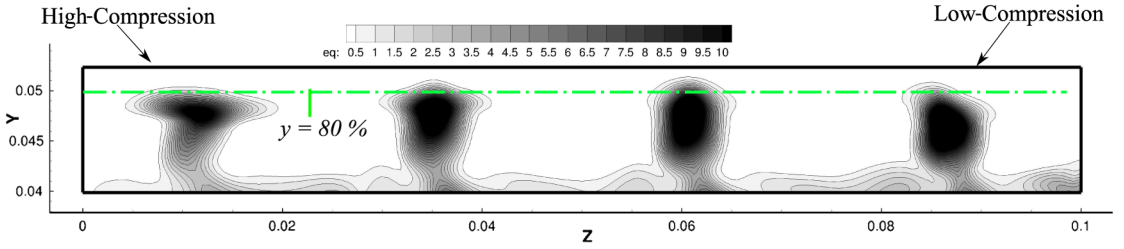

b) Cross-stream slice at entrance of combustor (x = 0.123 m): constant equivalence ratio contours

Fig. 18 3-D frozen results.

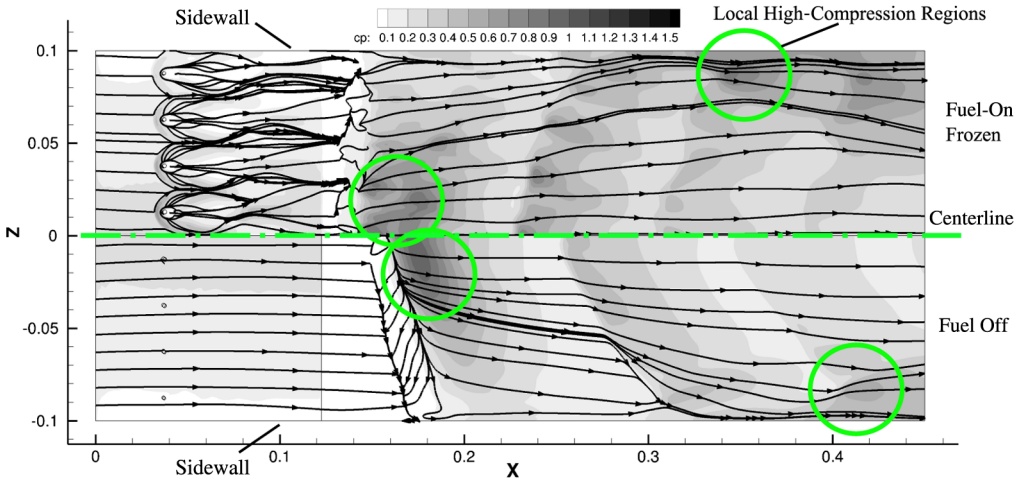

Fig. 19 Pressure bottom wall, fuel-on frozen (top), and fuel off (bottom): circles show high-pressure region at first SBLI and from spanwise reflection at sidewall.

$$I_{sp} = [(\dot{m}_5 U_5 - \dot{m}_0 U_0) + A_5(p_5 - p_0)]/\dot{m}_{H_2} g \qquad (5)$$

The upper part of Fig. 24 provides the uninstalled I_{sp} potential[‡‡] of the scramjet, assuming an isentropic nozzle expansion ratio (ER) of eight, calculated using Eq. (5), throughout the combustor. The improved uninstalled I_{sp} potential reflects the performance benefits of the increased pressure due to 3-D combustion phenomena in the 3-D engine. The performance enhancement occurs at the same streamwise location to the increased pressure and combustion efficiency at $x \approx 0.25$–0.35 m. The flow nonuniformity delivered to the exit of the combustor in the 3-D engine may degrade the performance relative to the 2-D engine, owing to additional losses incurred during the expansion process ([7] p. 388). To evaluate this, a nozzle with an expansion of 12 deg is added to the configurations. (Angles other than 12 deg can be used. A 12 deg expansion did not result in any boundary-layer separations, and is therefore considered sufficient to quantify the losses associated with expansion.) The nozzle geometry is given in Fig. 25. The bottom wall is modeled as an isothermal wall at 300 K. The uninstalled I_{sp} through the 2-D and 3-D engines are given in Fig. 25. The uninstalled I_{sp} of the 3-D engine is 221 s, which is higher compared to the 2-D engine of 121 s. Note that the uninstalled I_{sp} with a realistic nozzle is, naturally, lower than the uninstalled I_{sp} potential. The result highlights that the benefits from the increased combustion from the 3-D inlet-induced spanwise gradients outweigh the additional losses associated with the expansion process. Here, we have used a generic, nominally 2-D nozzle geometry; however, in practice, the 3-D engine may be designed with a 3-D nozzle that takes advantage of the nonuniformity. For example, the expansion process could be initiated after the spanwise reflection at the low-compression side. Such a concept will be the subject of future investigations.

An overview of the engine parameters of both engines is given in Table 4. The exit pressure coefficient c_p, combustion efficiency η_c,

[‡‡]The uninstalled I_{sp} potential does not account for the pressure (wave) or viscous drag generated on the external surface of the scramjet.

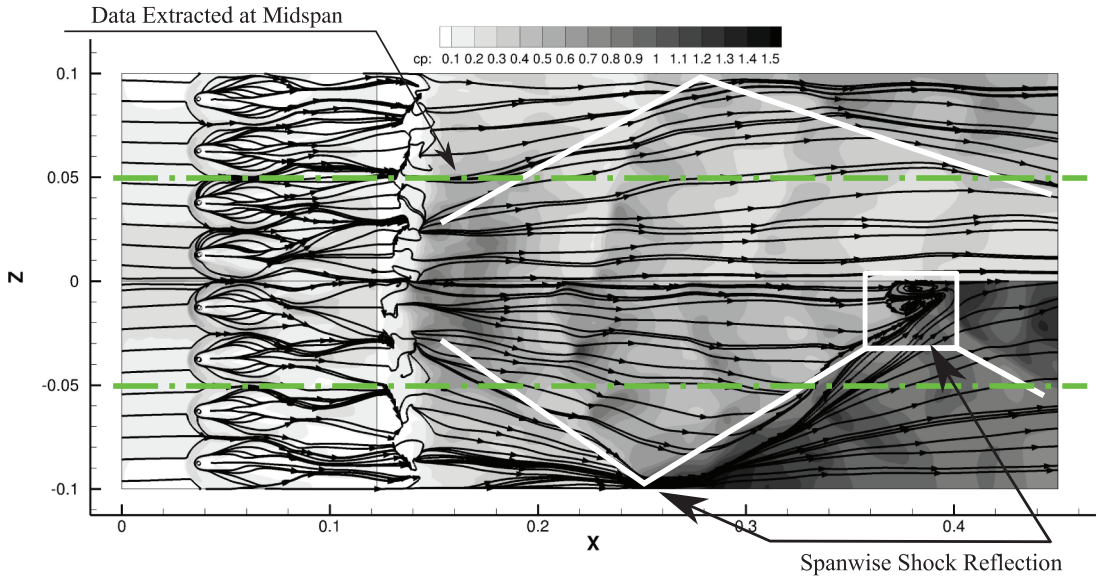

a) Fuel-on frozen and reacting flow pressure coefficient contours and shear stress topology along bottom wall

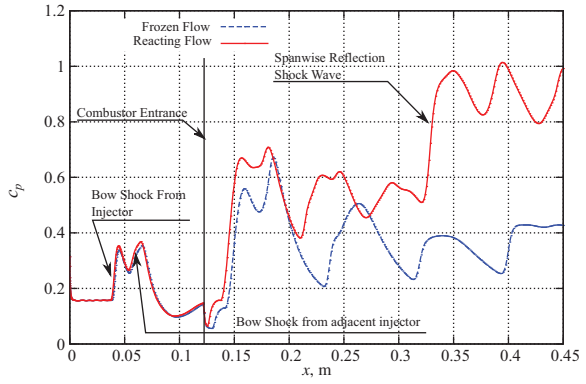

b) Pressure coefficient, data extracted at $z = 0.05$

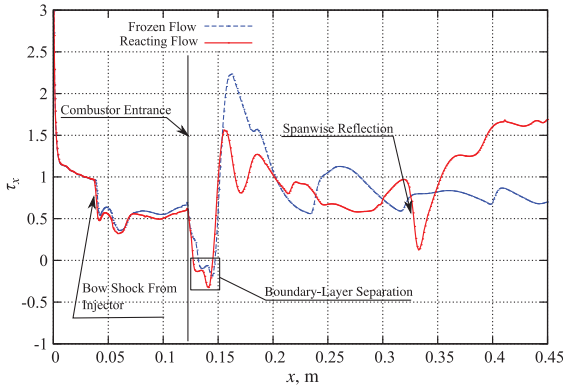

c) Shear stress (in kPa) data extracted at $z = 0.05$

Fig. 20 Fuel-on frozen and reacting flow, bottom wall shear stress topology, and pressure coefficient.

and uninstalled I_{sp} potential of the 3-D engine are greater than or equal to the 2-D engine in each case. The gain in combustion performance, pressure rise, and uninstalled I_{sp} potential in the 3-D engine is due to the TC, which is investigated in detail in the sections that follow. The potential I_{sp} from the nozzle surface for the 2-D and 3-D engines is 1325 and 1525 s, respectively, which is an increase of about 14%.

Owing to the generic (nonoptimized) scramjet configurations used in this study, the resulting combustion efficiencies of 57 and 66% in the 2-D and 3-D engines, respectively, are modest, even with the benefits of the thermal compression effect in the 3-D engine. The increase in combustion of 9% may therefore not be representative of properly configured (optimized) engines for this flight condition. The result, however, shows the combustion in the generic 3-D engine

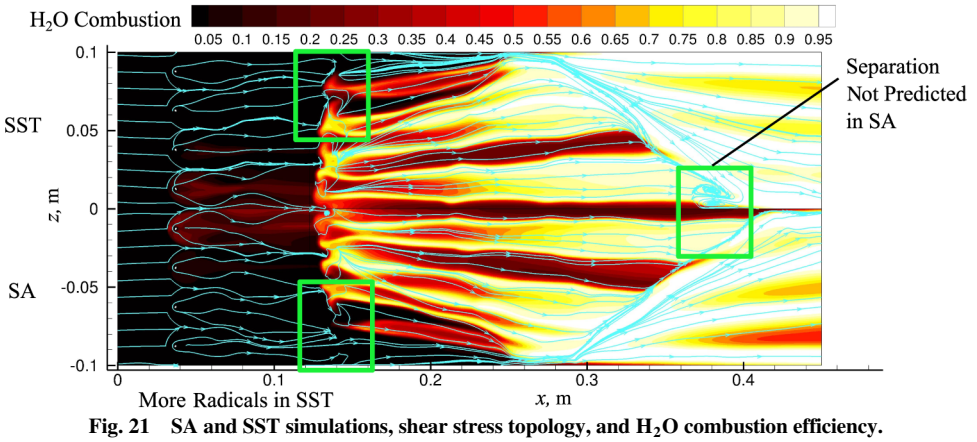

Fig. 21 SA and SST simulations, shear stress topology, and H_2O combustion efficiency.

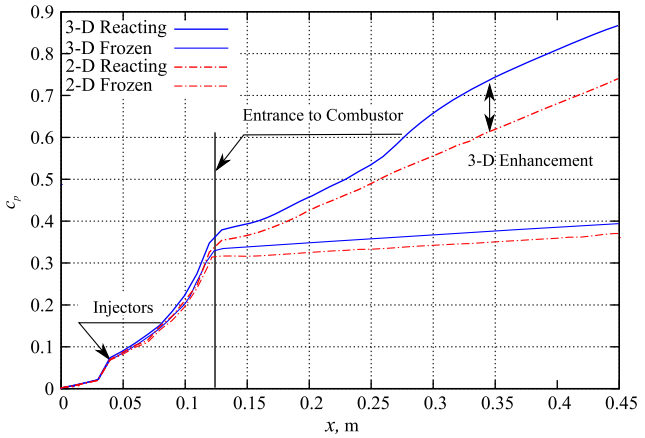

Fig. 22 Pressure rise within 3-D and 2-D engines.

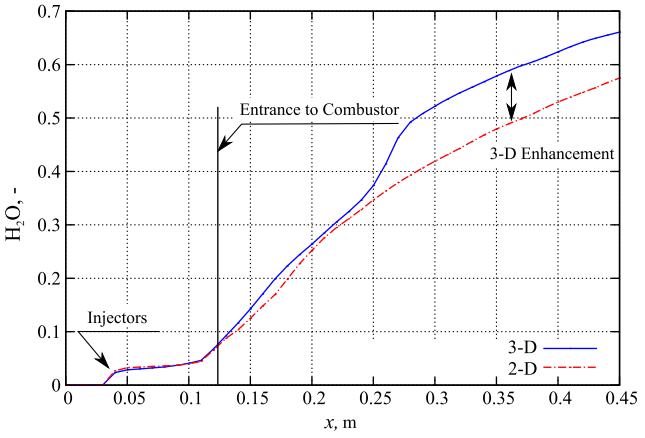

Fig. 23 H_2O combustion efficiency in 2-D and 3-D engines.

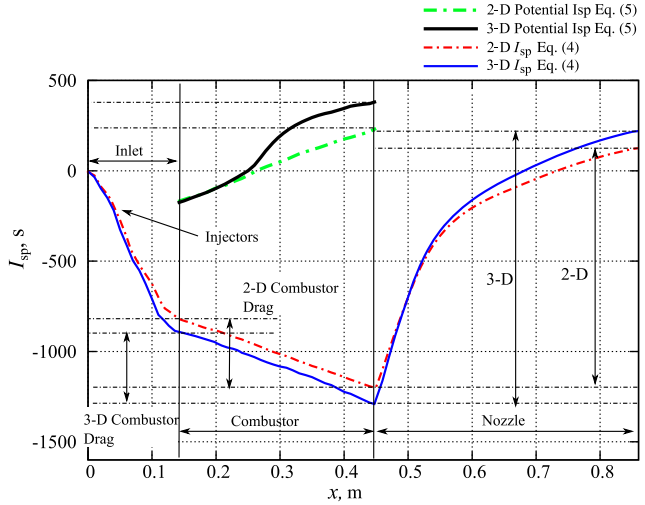

Fig. 24 Uninstalled I_{sp} breakdown ($x = 0$–0.86 m) and potential throughout combustor ($x = 0.123$–0.45 m) of 2-D and 3-D configurations assuming an ER of eight.

improves relative to the 2-D engine and suggests that TC is a useful mechanism to consider in the design of a practical scramjet engine at high Mach numbers. A study into the application of this work to practical scramjet configurations will be the subject of future investigations.

IX. Isolating Combustion Processes

The combustion processes discussed in the previous sections are now investigated in isolation. Further numerical simulations are conducted to determine how they influence the overall combustion behavior of the 3-D engine. Three fluid-dynamic/combustion interactions that facilitate ignition and combustion within the 3-D engine are identified as 1) 3-D flow features within the combustor: in particular, the influence of the SIBLS at the first SBLI and the spanwise reflections at the sidewall, 2) radical production from the injection method within the inlet, and 3) thermal compression, in the form of coupling of the spanwise flow gradients with combustion-induced compression waves.

The same interactions were identified in [15], excluding the radical production from the injection method. That paper showed TC-enhanced combustion within the low-compression side of the engine. In addition, a 3-D SIBLS ignited the flow in locally high-temperature regions in the boundary layer and transported radicals from the high- to low-compression sides of the engine.

Each interaction will be isolated by 1) comparing fuel-on frozen and reacting simulations, 2) injecting combinations of inert and reacting hydrogen within the high- and low-compression sides of the scramjet, and 3) artificially suppressing heat release in local regions. The results from these simulations are presented in Figs. 26 and 27. The pressure contours and shear stress topology show how the heat release influences the spanwise shock structures. The H_2O contours show where the flow ignites from within the boundary layer by 3-D flow features. Injecting reacting fuel into only the high- or low-compression side of the engine enables us to isolate how the fuel injected in each side burns without the influence of combustion from the other side. Injecting inert H_2 within the nonreacting side of the engine preserves the 3-D flow structures generated by the injection method.[§§] The injection method introduces additional shock structures into the engine, which in turn influence the behavior of the SIBLS, and therefore the combustion. Moreover, the injection method increases the effective compression ratio of the inlet. This compression needs to be conserved when comparing the pressure rise relative to the fuel-on frozen solutions, as shown in Fig. 26. The final method used to decouple the combustion processes is to artificially suppress reactions in local regions. This technique was used successfully in the premixed investigation [15]. This technique is useful here to remove the influence of radicals that form within the inlet and to isolate the combustion enhancement from TC within the low-compression side of the engine.

A. Three-Dimensional Flow Features

The influence of the SIBLS and spanwise flow reflection on combustion is isolated by injecting inert hydrogen and reacting hydrogen in only the low-compression (injectors 3 and 4) and high-compression (injectors 1 and 2) sides of the engine. These simulations are given in Figs. 26b, 26c, 27a, and 27b.

The high-compression-fueled simulation in Fig. 27b shows how the fuel injected in the high-compression side ignites without the influence of combustion of fuel injected in the low-compression side. The combustion between the first and second SBLIs in the high-compression side is unchanged relative to the fully fueled simulation. This indicates combustion in the high-compression side is not affected by the combustion of fuel injected in the low-compression side. There is H_2O present within the SIBLS in the low-compression side of the combustor, where only inert H_2 fuel is injected. Moreover, the second SBLI interaction transports the flow within the boundary layer further into the low-compression side where H_2O is present at the spanwise location $z = 0.095$ m at $x = 0.28$–0.33 m.

The low-compression-fueled result in Fig. 27a shows how the fuel injected in the low-compression side ignites without the influence of combustion from fuel injected in the high-compression side. The amount of H_2O in the boundary layer between the first and second SBLIs in the low-compression side is lower compared to the fully

[§§]In practice, an inert species with properties similar to hydrogen, such as helium, can be used to conduct experiments.

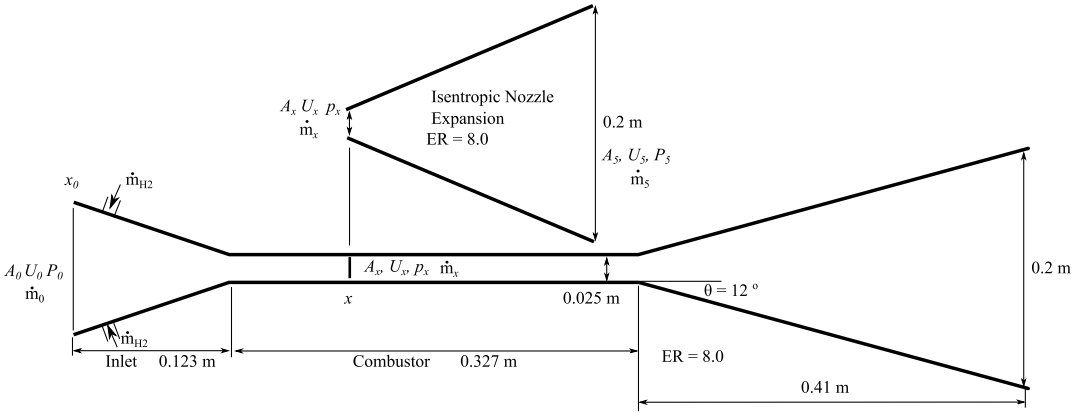

Fig. 25 Schematic of scramjet showing the expansion processes used to calculate uninstalled I_{sp} potential and actual uninstalled I_{sp} of the engine with an ER of eight.

fueled simulation. This indicates there is combustion enhancement in the low-compression side from combustion of fuel injected in the high-compression side. The enhancement is caused by radicals being transported within the SIBLS from the high- to the low-compression sides. This can be visualized in Fig. 28, where streamlines are entrained in and expelled out of the SIBLS. A similar combustion process was identified in the premixed investigation [15] and termed "radical transport," where it was also shown to enhance combustion in the low-compression side. The low-compression-fueled result shows significant combustion after the spanwise flow reflection at the sidewall, regardless of combustion in the high-compression region. This is due to a local high-pressure region that forms from the spanwise reflection. There is coupling of combustion-induced compression waves and the spanwise shock structure after the second SBLI, as shown by the change in the pressure contours and reflected shock structure angle in Figs. 26a and 26b.

The H_2O combustion contours and shear stress topology within the boundary between the premixed [15] and fully fueled simulation is given in Fig. 29 to highlight the affect of fuel injection on the ignition process within the SIBLS. The combustor length of the premixed simulation has been extended here from 0.3 to 0.45 m. Both simulations show that the flow along the bottom wall ignites from within the first SBLI. There are local changes to the SIBLS characteristics with injection caused by the additional shock structures and mixing processes. Higher levels of H_2O are produced in SIBLS with injection, due to the longer residence time of flow within the recirculation zones that result from the corrugated shape of the separation. Both simulations show coupling between the spanwise gradients and combustion. Unlike the injection simulation, however, the spanwise shock reflection in the premixed simulation does not traverse the entire width of the engine.

B. Radical Production from Injection Method

The influence of the radical production from the injection method is isolated by suppressing reactions in the inlet (Figs. 26e and 27d).

Table 4 Reacting flow combustor entrance and exit conditions of 2-D and 3-D engine configurations

STA property	2-D	3-D
c_p entrance	0.34	0.36
p_r inlet	22.5	23.5
c_p exit	0.74	0.87
η_c exit	0.57	0.66
η_M entrance, %	26	26
I_{sp} potential [Eq. (5)]	240	382
I_{sp} 12 deg expansion	121	221
ϕ	0.99	0.99

The reactions that take place in the inlet increase the pressure of the flow by 10% at the combustor entrance, as shown by the difference between the frozen and reacting STA pressure data in Fig. 22. The reactions-suppressed simulation (Fig. 27d) shows that the spanwise/combustion coupling behavior remains unchanged relative to the fully reacting simulation (Fig. 27c). The spanwise reflections at the sidewall and centerline move downstream 0.03 m relative to the fully reacting simulation. This is because suppressing radical production hinders the ignition of the flow in the combustor, and therefore the rate of heat release and pressure rise. Less pressure rise results in weaker coupling of the combustion-induced pressure waves with the spanwise flow gradients. The result highlights that the 3-D combustion/spanwise coupling behavior is independent of the radical production from the injection method. This indicates that the same flow behavior will most likely persist for other injection schemes that deliver a partially premixed flow to the combustor entrance.

C. Thermal Compression

The 3-D engine experiences an increase in the rate of pressure rise around the second SBLI and spanwise reflection, $x \approx 0.25$–0.33 m, as shown in Fig. 22. This increased rate of pressure rise is largely due to TC where combustion within the high-compression side compresses the flow in the low-compression side, thereby enhancing combustion. The presence of H_2O (and therefore radicals) at the second SBLI in the low-compression side enhances combustion [15]. The low-compression-fueled simulation (Fig. 27a) shows that combustion (and therefore radical production) takes place in the low-compression side upstream of the second SBLI. The high-compression-fueled simulation (Fig. 27b) shows that combustion products are transported into the low-compression side from fuel injected into the high-compression side. The influence of these radicals on the combustion at the second SBLI must be removed if we are to isolate the combustion enhancement from only TC. This is achieved using two reaction suppression regions, specified in Table 5: region 1 is used to suppress radicals forming upstream of the second SBLI in the low-compression side. Region 2 is used to suppress the production of the radicals that are transported within the boundary layer from the high- to the low-compression sides. TC can now be isolated by comparing the results of the low-compression, high-compression, and fully fueled simulations with the reaction suppression regions, given in Fig. 30.

The low-compression-fueled simulation (Fig. 30a) shows the fuel injected in the low-compression side (injectors 3 and 4) ignites at the spanwise reflection at $x \approx 0.33$ m, given by the bottom-wall H_2O combustion contours. The high-compression-fueled simulation (Fig. 30b) shows the region in the low-compression side where no H_2O is transported from fuel injected in the high-compression side. (By comparing the high-compression fueled with (Fig. 30b) and without (Fig. 27b) reaction suppression in region 2, we see that the area without radicals increases. This enables us to isolate the influence of TC on combustion on a greater portion of the flow in the

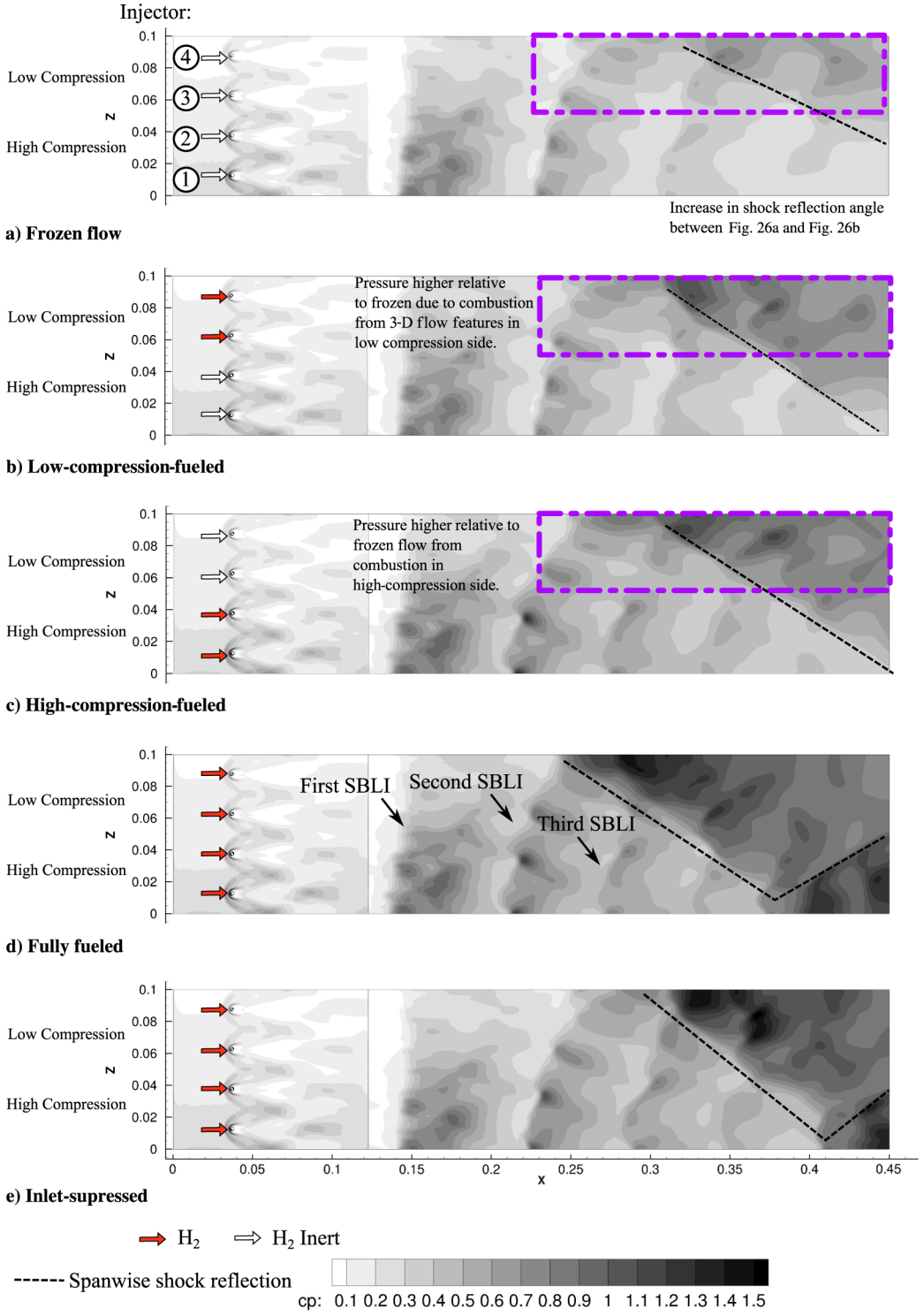

Fig. 26 Pressure contours along the bottom wall for high-compression, low-compression, fully fueled, and inlet-suppressed simulations.

low-compression side.) The fully fueled simulation (Fig. 30c) shows combustion in the low-compression side is achieved at $x \approx 0.25$ m, further upstream compared to the low-compression-fueled simulation, and in the region where no H_2O transport from fuel injected in the high-compression side is possible (see Fig. 30b.) This result shows that TC from combustion in the high-compression side between the first and second SBLIs enhances combustion of the fuel injected in the low-compression side of the engine.

The cross-stream slices of H_2O combustion efficiency in Fig. 31 show how the core flow is ignited in both the low-compression and fully fueled simulations. Figure 31a shows the fuel plumes in the low-compression side ignite at $x = 0.38$ m, as opposed to Fig. 31a (with TC), which ignites upstream at $x = 0.32$ m. The heat release in the low-compression region (with TC) occurs at a higher pressure and temperature, as well as a lower Mach number, and therefore at a higher thermodynamic efficiency. (For a given amount of heat release, the lower the local Mach number, the higher the thermal efficiency. This is explained by Rayleigh losses (see, for example, [7] p. 77).) We have not investigated the effects that TC and flow nonuniformity have on the mixing processes in the combustor. Another aspect not investigated in this work is the relative unstart behavior and engine operability between an optimized TC and an

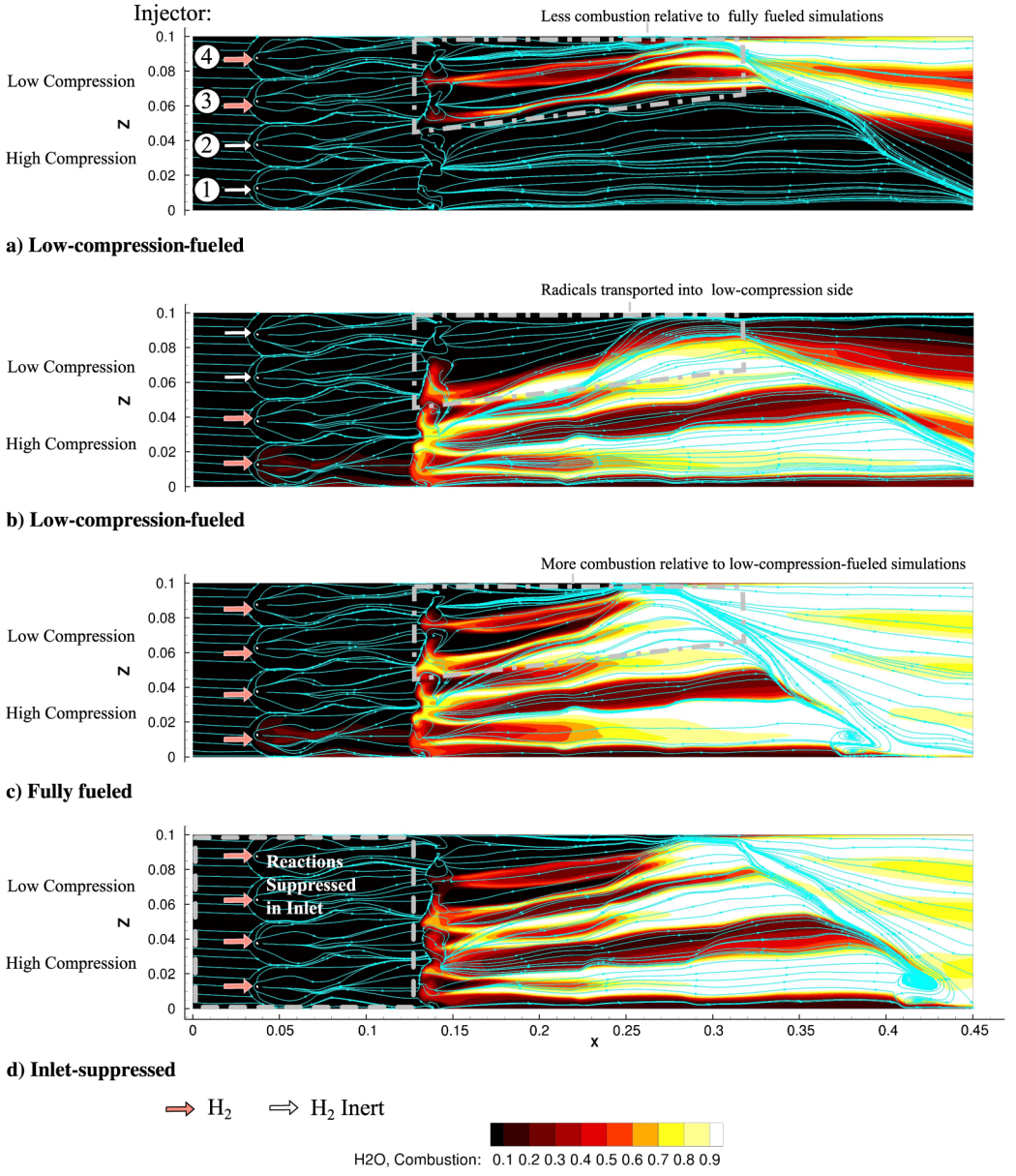

Fig. 27 H_2O combustion contours along the bottom wall for high-compression, low-compression, fully fueled, and inlet radical suppressed simulations.

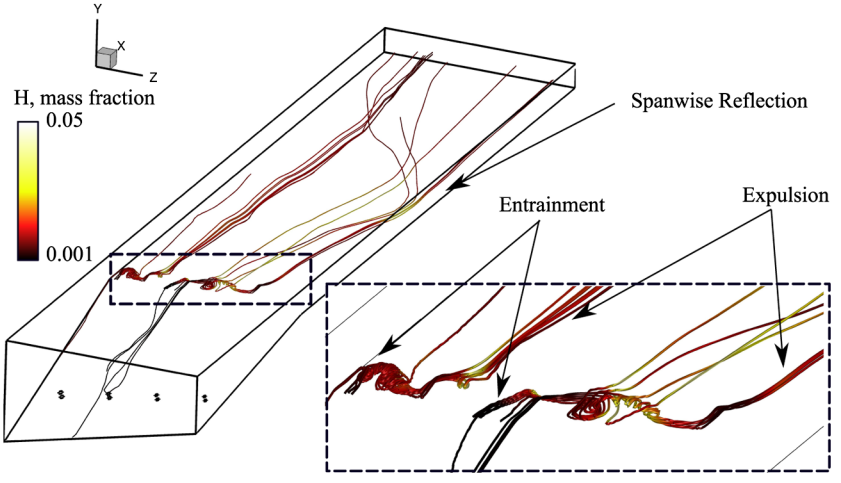

Fig. 28 Fully reacting flow, entrainment, and expulsion of streamlines within SIBLS: streamlines flooded with atomic hydrogen mass fraction.

Table 5 Reaction suppression regions

Position	Region 1	Region 2
x_{min}	0.0	0.123
x_{max}	0.25	0.25
y_{min}	0	0.39
y_{max}	0.52	0.43
z_{min}	0.05	0.05
z_{max}	0.1	0.06

optimized 2-D engine, which remains an open question. For example, it is unknown at this time whether the coupling between the nonuniform compression with combustion waves will lead to a degradation of the isolator–inlet–combustor operability compared with the 2-D engine. Assessment of the unstart characteristics of this class of engine will be an important aspect for future studies that seek to develop an operational scramjet concept using the TC effects uncovered here.

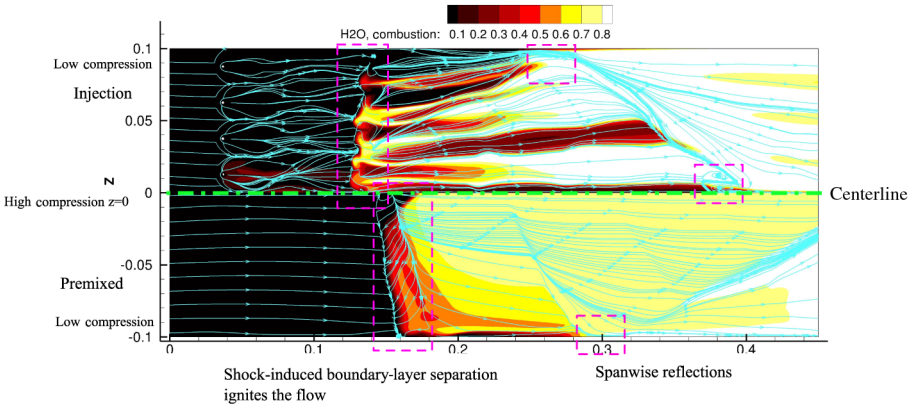

Fig. 29 Comparison of fully fueled simulation (present study) and premixed study [15]: bottom wall flooded with H_2O combustion contours and shear stress topology.

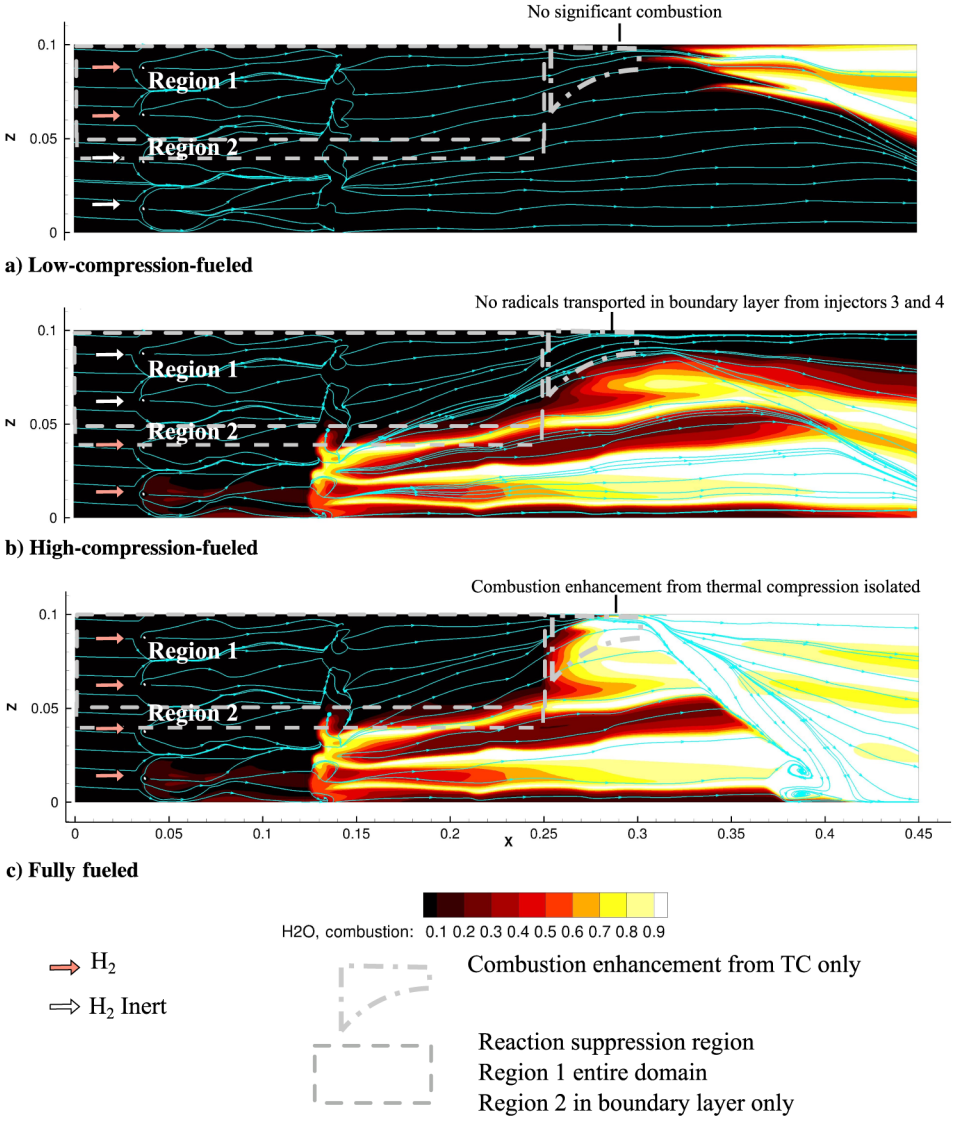

Fig. 30 Isolating TC within the low-compression side of the 3-D engine.

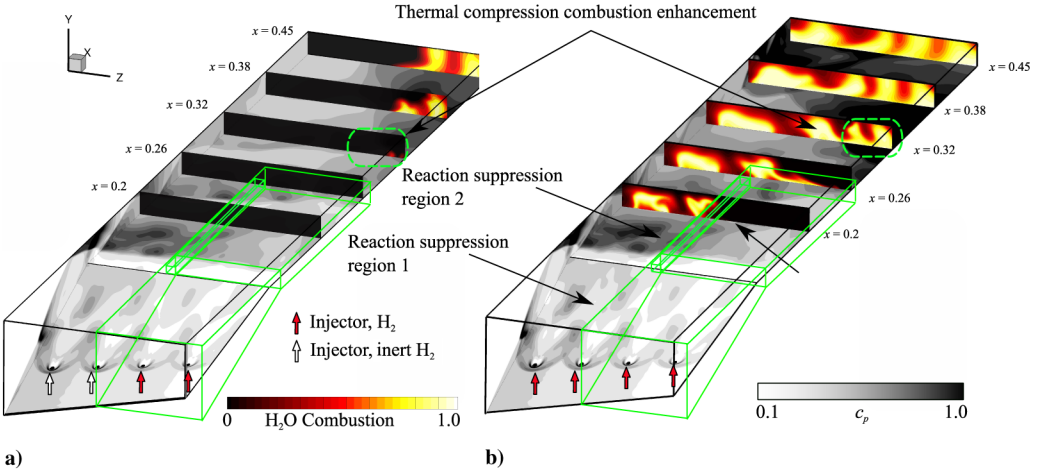

Fig. 31 Isolating TC within the low-compression side of 3-D engine.

X. Conclusions

This paper is an extension of a fundamental study of a premixed three-dimensional nonuniform-compression scramjet that showed thermal compression and 3-D flow features-enhanced combustion. The paper demonstrates that TC can be used in a realistic inlet-fueled 3-D nonuniform-compression scramjet configuration. Such a scramjet offers an additional degree of freedom in the design process of fixed-geometry scramjets that must operate over a range of flight Mach numbers. The uninstalled I_{sp} of the 3-D engine improves compared to a nominally two-dimensional engine of about the same contraction and compression ratios. The 3-D combustion processes become more complex compared to those identified in the premixed study due to the additional shock structures introduced from the injection method and associated mixing processes. Although these effects impart local changes to the flow, they do not affect the global combustion behavior. As in the previous premixed study, the flow in the boundary layer ignites from within the shock-induced boundary-layer separation that forms at the entrance to the combustor. The TC effect from the coupling of combustion-induced compression waves with the inlet-induced spanwise flow gradients enhances combustion. Radicals that form upstream from the combustor within the free shear layer of the injector plume and air enhance combustion. Suppressing the production of radicals in the inlet does not change the global combustion behavior. The findings demonstrate that the global 3-D combustion behavior is not unique to this injection scheme. The technique is expected to be applicable to other inlet-fueling injection schemes that deliver partially mixed fuel and air to the combustor.

Acknowledgments

This research was funded by the Australian Space Research Program project titled "Scramjet-Based Access For Space Systems." This work was supported by the University of Queensland and by computational resources of the National Computational Infrastructure National Facility through the National Computational Merit Allocation Scheme.

References

[1] Hirschel, E., and Weiland, C., *Selected Aerothermodynamic Design Problems of Hypersonic Flight Vehicles*, Springer, New York, 2009, p. 131.

[2] Smart, M., and Tetlow, M., "Orbital Delivery of Small Payloads Using Hypersonic Airbreathing Propulsion," *Journal of Spacecraft and Rockets*, Vol. 46, No. 1, 2009, pp. 117–125. doi:10.2514/1.38784

[3] Billig, F., Orth, R., and Lasky, M., "Effects of Thermal Compression on the Performance Estimates of Hypersonic Ramjets," *Journal of Spacecraft*, Vol. 5, No. 9, 1968, pp. 1076–1081. doi:10.2514/3.29424

[4] Drummond, J., Diskin, G., and Cutler, A., "Fuel-Air Mixing and Combustion in Scramjets," *38th AIAA/ASME/SAE/ASEE Joint Propulsion Conference and Exhibition*, AIAA Paper 2002-3878, 2002.

[5] Billig, F., "Combustion Processes in Supersonic Flow," *Journal of Propulsion and Power*, Vol. 4, No. 3, 1988, pp. 209–216. doi:10.2514/3.23050

[6] Ferri, A., "Review of SCRAMJET Propulsion Technology," *Journal of Aircraft*, Vol. 5, No. 1, 1968, pp. 3–10. doi:10.2514/3.43899

[7] Heiser, W., and Pratt, D., *Hypersonic Airbreathing Propulsion*, AIAA, Washington, D.C., 1994, p. 39.

[8] Smart, M., "How Much Compression Should a Scramjet Inlet Do?" *AIAA Journal*, Vol. 50, No. 3, 2012, pp. 610–619. doi:10.2514/1.J051281

[9] Ferri, A., "Mixing Controlled Supersonic Combustion," *Annual Review of Fluid Mechanics*, Vol. 5, Jan. 1973, pp. 301–338. doi:10.1146/annurev.fl.05.010173.001505

[10] Ferri, A., and Fox, H., "Analysis of Fluid Dynamics of Supersonic Combustion Process Controlled by Mixing," *International Symposium on Combustion*, Vol. 12, No. 1, 1969, pp. 1105–1113. doi:10.1016/S0082-0784(69)80488-1

[11] Van Wie, D., Kwok, F., and Walsh, R., "Starting Charateristics of Supersonic Inlets," AIAA Paper 1996-2914, 1996.

[12] Curran, E., "Scramjet Engines: The First Forty Years," *Journal of Propulsion and Power*, Vol. 17, No. 6, 2001, pp. 1138–1148. doi:10.2514/2.5875

[13] Peschke, W., "Approach to In Situ Analysis of Scramjet Combustor Behavior," *Journal of Propulsion and Power*, Vol. 11, No. 5, 1995, pp. 943–949. doi:10.2514/3.23921

[14] Erdos, I., and Nucci, M., "Pioneering Scramjet Developments by Antonio Ferri," General Applied Science Labs TR N92-21519, Ronkonkoma, NY, 1992.

[15] Bricalli, M., Boyce, R., and Brown, M., "Supersonic Combustion Processes in a Premixed Three-Dimensional Nonuniform-Compression Scramjet Engine," *AIAA Journal*, Vol. 52, No. 8, 2014, pp. 1670–1685. doi:10.2514/1.J052640

[16] Ferri, A., and Agnone, A., "Heat Conduction Controlled Combustion for Scramjet Applications," NASA TR CR-123446, 1970.

[17] Gardner, A., Paull, A., and McIntyre, T., "Upstream Porthole Injection in a 2D Scramjet Model," *Shock Waves*, Vol. 11, No. 5, 2002, pp. 369–375. doi:10.1007/s001930200120

[18] Odam, J., and Paull, A., "Radical Farming in Scramjets," *Notes on Numerical Fluid Mechanics and Multidisciplinary Design (NNFM)*, Vol. 96, 2008, pp. 276–283. doi:10.1007/978-3-540-74460-3_34

[19] McGuire, J., Boyce, R., and Mudford, N., "Radical-Farm Ignition Processes in Two-Dimensional Supersonic Combustion," *Journal of Propulsion and Power*, Vol. 24, No. 6, 2008, pp. 1248–1257. doi:10.2514/1.35562

[20] Turner, J., and Smart, M., "Application of Inlet Injection to a Three-Dimensional Scramjet at Mach 8," *AIAA Journal*, Vol. 48, No. 4, 2010, pp. 829–838. doi:10.2514/1.J050052

[21] Goldberg, U., Batten, P., Palaniswamy, S., Chakravarthy, S., and Peroomian, O., "Hypersonic Flow Predictions Using Linear and Nonlinear Turbulence Closures," *Journal of Aircraft*, Vol. 37, No. 4, 2000, pp. 671–675. doi:10.2514/2.2650

[22] Menter, F. R., Kuntz, M., and Langtry, R., "Ten Years of Industrial Experience with the SST Turbulence Model," *Turbulence, Heat and Mass Transfer 4*, edited by Hanjalic, K., Nagano, Y., and Tummers, M., Begell House, Danbury, CT, 2003, pp. 625–632.

[23] Reinartz, B., "Parametric Study for Scramjet Intake Concerning Wall Temperatures and Turbulence Modeling," *High Performance Computing in Science and Engineering*, Springer–Verlag, Berlin, 2012, pp. 425–436.

[24] Pudsey, A., Boyce, R., and Wheatley, V., "Influence of Common Modeling Choices for High Speed Transverse Jet Interaction Simulations," *Journal of Power and Propulsion*, Vol. 29, No. 5, 2013, pp. 1079–1086. doi:10.2514/1.B34750

[25] Jachimowski, C., "An Analysis of Combustion Studies in Shock Expansion Tunnels and Reflected Shock Tunnels," NASA Langley Research Center TR-3224, 1992.

[26] Povinelli, F., and Povinelli, L., "Correlation of Secondary Sonic and Supersonic Gaseous Jet Penetration into Supersonic Crossflows," NASA TN-D-6370, 1971.

[27] GridPro, Software Package, Ver. 5.1, Program Development Corp, White Plains, NY, 2011.

[28] Doster, J., King, P., Gruber, M., Carter, C., Ryan, M., and Hsu, K., "In-Stream Hypermixer Fueling Pylons in Supersonic Flow," *Journal of Propulsion and Power*, Vol. 25, No. 4, 2009, pp. 885–901. doi:10.2514/1.40179

[29] Peterson, D., Boyce, R., and Wheatley, V., "Simulations of Mixing in an Inlet-Fueled Axisymmetric Scramjet," *AIAA Journal*, Vol. 51, No. 12, 2013, pp. 2823–2832. doi:10.2514/1.J052480

[30] Gehre, R., Peterson, D., Wheatley, V., and Boyce, R., "Numerical Investigation of the Mixing Process in Inlet Fuelled Scramjets," *29th International Symposium on Shock Waves*, Madison, WI, 2013.

[31] Ben-Yakar, A., and Hanson, R., "Supersonic Combustion of Cross-Flow Jets and the Influence of Cavity Flame-Holders," AIAA Paper 1999-0484, 1999.

[32] Spalart, R. R., and Allmaras, S. R., "A One-Equation Turbulence Model for Aerodynamic Flows," *La Recherche Aerospatiale*, Vol. 17, No. 1, 1994, pp. 5–21.

[33] Gollan, R., "Onedval: A Tool to Extract One-Dimensionalised Properties from CFD Data," Univ. of Queensland Mechanical Engineering Rept. 2013/04, Brisbane, QLD, Australia, 2013.

[34] Baurle, R., and Gaffney, L., "Extraction of One-Dimensional Flow Properties from Multidimensional Data Sets," *Journal of Propulsion and Power*, Vol. 24, No. 4, 2008, pp. 704–714. doi:10.2514/1.32074

J. Drummond
Associate Editor